Eindhoven University of Technology

BACHELOR

Modeling fluctuations of single pedestrian dynamics on curved paths

van der Vleuten, Geert G.M.

Award date:
2021

Eindhoven University of Technology
Department of Applied Physics &
Department of Applied Mathematics
Fluids and Flows

Modeling fluctuations of single pedestrian dynamics on curved paths

Bachelor Thesis

Geert van der Vleuten
1260758

R-2043 SB

Supervisors:
dr. A. Corbetta
prof. W. Schilders
prof. F. Toschi

Final version

Eindhoven, January 2021

Abstract

In an urbanizing modern day society the modeling of pedestrian dynamics has many fields of applications such as city infrastructure design and safety planning. One way to model diluted, single pedestrian flows is force-based modeling. This method expresses the individual dynamics in an interplay of, so called, "social forces". The problem is reasonably well understood when it comes to modeling of individual dynamics along straight paths in terms of the typical fluctuations that such motions feature. This thesis proposes a model that quantitatively reproduces the fluctuations of single pedestrian dynamics on curved base-paths. Modeling forces are used to confine pedestrians to a motion and account for the stochastic behaviour of pedestrians. A covariant derivative is introduced that enables a natural generalization of the force-based straight path dynamics to curved paths. Several differential geometry concepts are used to accomplish this. The model is quantitatively validated with two real life experiments. Compared are the empiric and simulated distributions of velocity and position fluctuations. The comparison of the model with the experiments shows good resemblance with real life pedestrian dynamics limited to the diluted scenario.

Table of Contents

1. Introduction

More than half of the world population lives in cities [1]. United Nation studies suggest that this portion grows towards 75% in 2050 [2]. Meanwhile, this is only 3% of the planet's land surface. This massive influx to the urban-population will not contribute to the fluency in which people flow through the city. Consequences of large and dense crowd flows can be accidents, congestions (Figure 1.1), queues and traffic jams. With pedestrian traffic as main traffic in cities, it is important that the flows of pedestrians are smooth.

Figure 1.1: A crowded junction at the Shibuya station, Tokyo. *Source: Sean Pavone/Shutterstock.*

In order to control these flows, it is important to understand the dynamics of single pedestrians. The behaviour of pedestrians, whether as crowds or as individuals, can be modeled. These models help to predict how pedestrian flows will react to certain situations. Examples of applications are city planning and evacuation planning [3].

The modeling of pedestrian dynamics has numerous fields of research. This thesis focuses on the modeling of typical fluctuations that pedestrian motions feature. A common way of doing so is describing pedestrian motions as if they would be subject to, so called "social forces". This has already been applied to straight paths [4]. However, paths of pedestrians are not generally straight. In this thesis, a model is proposed that quantitatively reproduces fluctuations of single pedestrians around generic curved base-paths.

For curved base-paths, the dynamics become very complex. Therefore, base-paths are taken to be geodesics. Geodesics are paths that a person would follow if he keeps going straight ahead. In our physical space geodesics are straight lines. But if the geometry is changed, geodesics are no longer necessarily straight lines. For switching between the different geometries, differential geometry tools are needed.

The conceptual frame work is presented in Chapter 2 in order to create a good intuitive understanding of the modeling idea. All technical aspects, among others the differential geometry tools, that has to be understood are explained in the theoretical background (Chapter 3). Subsequently, the model is proposed in Chapter 4. The simulation procedure is discussed in Chapter 5. After this, the model is validated. In this chapter, the model is quantitatively compared with two real life experiments. The results are discussed and a conclusion is drawn in Chapter 7.

2. Conceptual framework

In this chapter, the modeling concept is explained and the challenge for this thesis becomes clear. The conceptual framework creates a better understanding of the subject.

Suppose a ball is given a kick on a flat surface in a force free environment. The ball would follow a straight path. The motion of the ball is governed by Newton's second law:

$$\vec{F} = m\vec{a}. \tag{2.1}$$

In Equation (2.1), m and $\vec{a}$ are the mass and acceleration respectively and $\vec{F}$ represents the sum of all forces active on the mass. The ball that was kicked on the flat surface does not experience any forces so it has constant velocity ($a = 0$). If forces are added, the velocity's magnitude and direction can be changed and therewith the dynamics of the ball.

Force based modeling treats single pedestrians as active particles governed by Newtonian dynamics. This method uses force to model the dynamics of a particle.

Without forces, every particle follows straight paths. In reality, pedestrians perturb from these straight paths due to social forces, geometrical constraints or internal forces. Social forces are forces that guide behavioural changes [5]. Think, for instance, of a sidestep to go back to the path that you intend to follow or the avoidance of another pedestrian. The following question arises: which forces does a particle need to increase resemblance of its dynamics with a real life pedestrian?

A realistic model that describes the fluctuations of pedestrian dynamics quantitatively has already been proposed for diluted straight paths [4]. This model assumes that there is no correlation between the longitudinal and transversal dynamics. Therefore, the dynamics in the different directions are modeled independently according to

$$\begin{cases} \dot{x} = u & (2.2) \\ \dot{y} = v & (2.3) \\ \dot{u} = -4\alpha u(u^2 - u_p^2) + \sigma_x \dot{W} & (2.4) \\ \dot{v} = -2\beta y - 2\mu v + \sigma_y \dot{W} & (2.5) \end{cases}$$

Here, x, the longitudinal coordinate, and y, the transversal coordinate, are Cartesian coordinates with corresponding velocities u and v. In Equation (2.4) and (2.5), it can be seen that the acceleration in the different coordinate directions is determined with a collection of modeling forces.

The lateral dynamics are determined by three forces. The first two forces are the result of a harmonic confinement potential which consists of a position potential (Φ_y) and a velocity potential (Φ_v), where

$$\Phi_y(y) = \beta y^2 \quad \text{and} \quad \Phi_v(v) = \mu v^2. \tag{2.6}$$

These potentials cause the particle to move to the desired straight path when it is perturbed from it. The confinement potential well can be compared with an U-shaped slope. A visualization of this is shown in Figure 2.1a.

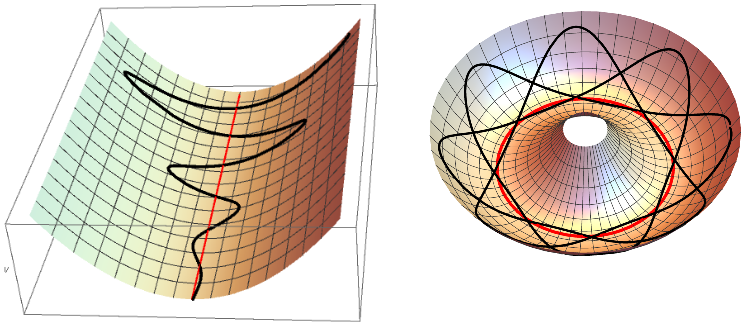

(a) **(b)**

Figure 2.1: Visualization of confinement potential with a trajectory that converges to a desired straight path (a). In (b): A circular potential with the desired circular path at its bottom. Visible are the spurious fluctuations in blue.

The third force that controls the lateral dynamics is a stochastic force. With purely deterministic dynamics, every particle with the same starting position and velocity will follow the same trajectory. However, in reality pedestrians might exhibit different trajectories when they have the same initial conditions. The third lateral force is random noise that should account for the stochastic behaviour that pedestrians have.

According to Equation (2.4), the longitudinal dynamics is controlled by two forces. The first modeling force is the longitudinal propulsion force is given by $f(u) = -4\alpha u(u^2 - u_p^2)$ and is the result of a longitudinal velocity potential (Φ_u), where

$$\Phi_u(u) = \alpha(u^2 - u_p^2)^2. \tag{2.7}$$

The longitudinal propulsion force keeps the particle moving around the same velocity in longitudinal direction. This desired velocity is represented by parameter u_p. The other parameter, α, is a scale parameter. When the particle is moving too slow or too fast, this force causes an acceleration or a deceleration respectively. Real life pedestrians also create this force intrinsically to overcome friction. The second force that determines the longitudinal dynamics is again random noise.

Equations (2.2)-(2.5) describe the dynamics of pedestrians along straight paths. A straight path is the result of force-free motion in flat space. In order to adapt this model for curved paths the first intuitive approach would be to extend the confinement potential along a curved path. This would mean that the particle is constantly forced to a desired curved path. Take for example a circle as desired curved path. In order to confine the particle to the circle, a circular harmonic potential can be added with the desired circle at its bottom. Suppose a ball is given a kick in an environment where solely the confinement force works on the ball. The ball will follow a path similar to the path shown in Figure 2.1b. It can be seen that the trajectory of the ball fluctuates along the base-path but the fluctuations stay on the outer side of the circle. This is a result of the curving of the potential. Since the fluctuations are expected to be symmetric on both sides of the circle, the fluctuations are spurious. Clearly this is not the way to adapt the model for curved base-paths.

An alternative approach is needed. Until now, straight lines were defined to be the result of force-free motion in flat space. What if a force-free motion is performed in curved space? The resulting path is no longer a straight line. Take, for example, the polar parametrization of $\mathbb{R}^2$. This is a simple and common coordinate system where the coordinate lines are curved. Figure 2.2 shows that a straight line in the polar parametrization looks like circle when it is observed in Cartesian coordinates. Straight lines can be redefined such that straight lines are the result of force-free motion in curved space. Consequently, paths that look curved can still satisfy the definition of a straight line. For example, if force-free paths in the polar parametrization (Figure 2.2b) are defined to be straight, the circle is in Figure 2.2a is also straight. As a result, the harmonic confinement potential in Figure 2.1b is now centered around a straight path. The fluctuation will no longer be spurious.

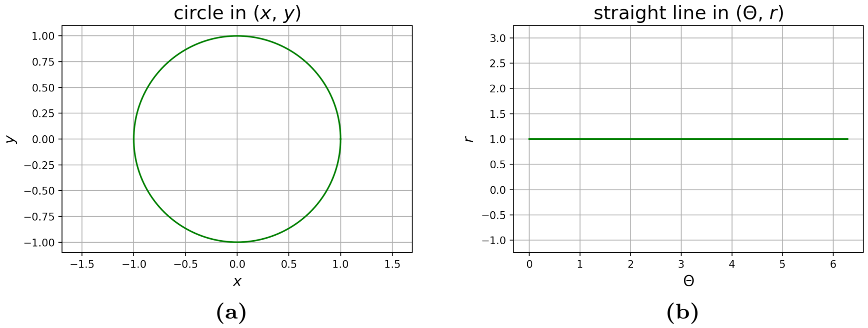

Figure 2.2: A circle in Cartesian coordinates (a) corresponds to a straight line in polar coordinates (b).

The discussed model for fluctuations of single pedestrian dynamics (Equations (2.2)-(2.5)) is intended for straight paths. If the concept 'straight' is defined wisely, any curved path can be straight. The mathematical field of differential geometry provides tools that are needed for the new definition of straight.

The redefinition of straight alters the acceleration vector $\vec{\alpha}$. With the new acceleration vector, the equation of motion based on Newton's second law could be derived. After that, modeling forces could be added to make the model more realistic.

3. Theoretical background

In this chapter, several technical and mathematical concepts will be elaborated that will be needed for the construction of the model.

3.1 Differential geometry

As explained in the conceptual framework (Chapter 2), differential geometry is the field of mathematics that is needed to make a connection between different parametrizations. Differential geometry uses techniques from calculus to investigate all kinds of properties of smoothly varying manifolds. In the following subsections, several concepts are discussed that are important for the understanding of the mathematical model.

3.1.1 Curvilinear coordinates

A point $\mathbf{x}$ in the n-dimensional Euclidean space ($\mathbb{R}^n$) are most often represented in its Cartesian coordinates $x^i \in \mathbb{R}$. That are the coordinates relative to the standard basis $\{\mathbf{e}_i \equiv \frac{\partial}{\partial x^i}\}, i = 1, 2, ..., n$, where $\mathbf{e}_i$ are the basis vectors with the i-th entry equal to 1 and the other entries equal to 0. As a result: $\mathbf{x} = x^i \mathbf{e}_i$. In the latter expression, the Einstein summation convention is used ($x^i \mathbf{e}_i \equiv \sum_i x^i \mathbf{e}_i$). The Einstein summation convention will also be used in the remainder of this report.

Sometimes, it is useful to use other coordinate systems. If a coordinates system does not have straight coordinate lines it is called a curvilinear coordinate system. Well known examples of curvilinear coordinates are spherical coordinates, cylindrical coordinates in $\mathbb{R}^3$ or polar coordinates in $\mathbb{R}^2$. Suppose a curvilinear coordinate system with basis $\{\hat{\mathbf{e}}_i\}, i = 1, 2, ..., n$. Point $\mathbf{x}$ can also be expressed in curvilinear coordinates: $\mathbf{x} = x^i \mathbf{e}_i = q^i \hat{\mathbf{e}}_i$, where q^i are the curvilinear coordinates.

The curvilinear basis vectors can easily be expressed in the standard basis vectors. This is a matter of chain-rule:

$$\hat{\mathbf{e}}_i = \frac{\partial}{\partial q^i} = \frac{\partial x^j}{\partial q^i} \frac{\partial}{\partial x^j} = \frac{\partial x^j}{\partial q^i} \mathbf{e}_j. \tag{3.1}$$

A differentiable manifold M is topological space that locally resembles an Euclidean space. A practical example is the surface of the earth that locally looks like $\mathbb{R}^2$. A more trivial example is $\mathbb{R}^2$ which locally resembles $\mathbb{R}^2$. Each coordinate system has a diffeomorphism ϕ_α that gives the coordinates of a region Ω_α on manifold M: $\phi_\alpha : \Omega_\alpha \subset M \to \mathbb{R}^n$. For instance, the map ϕ_x for the Cartesian coordinates maps a point $p \in M$ to its Cartesian coordinates: $\phi_x(p) = x \in \mathbb{R}^n$.

If two mappings cover an overlapping region on a manifold ($\Omega_\alpha \cap \Omega_\beta \neq \emptyset$), a smooth diffeomorphism or coordinate transformation exists between the two charts. This coordinate transformation is given by

$$\phi = \phi_\beta \circ \phi_\alpha^{-1} : \phi_\alpha(\Omega_\alpha \cap \Omega_\beta) \subset \mathbb{R}^n \to \phi_\beta(\Omega_\alpha \cap \Omega_\beta) \subset \mathbb{R}^n : x \mapsto y = \phi_\beta \circ \phi_\alpha^{-1}(x), \tag{3.2}$$

where $x, y \in \mathbb{R}^n$ are coordinates in coordinate chart ϕ_α and ϕ_β respectively [6]. Note that the coordinate charts $\phi_\alpha(\Omega_\alpha)$ and $\phi_\beta(\Omega_\beta)$ are denoted as ϕ_α and ϕ_β by abuse of notation.

3.1.2 Pull-back and push-forward

Suppose a smooth mapping between two manifolds M and N with $\dim M = \dim N = n$: $\phi : M \to N$. The map ϕ that maps points on M to points on N is called a push-forward. If ϕ is a diffeomorphism, the map can be reversed: $\phi^{-1} : N \to M$. The inverse mapping is used to pull-back points to manifold M. One can also think of manifolds M and N as two coordinate charts ϕ_α and ϕ_β. In this case, the coordinate transformation $\phi = \phi_\beta \circ \phi_\alpha^{-1}$ is used to push-forward coordinates.

As mentioned before, every point on a manifold locally resembles $\mathbb{R}^n$. When this Euclidean space is extended, a tangent space is created. For the example of the manifold that is the surface of the earth, the tangent space at a point p is the tangent plane ($\mathbb{R}^2$) at that point. For the trivial example of the flat plane, the tangent space at a point p is the same flat plane. A tangent space at point $p \in M$ is denoted as TM_p. The dimension of a tangent space is the same as the dimension of the manifold.

Vectors $\mathbf{v} \in \mathrm{TM} \subset \mathbb{R}^n$ can also be pushed-forward from manifolds M to manifold N. This is done with the map

$$\phi_* : \mathrm{TM}_p \subset \mathbb{R}^n \to \mathrm{TN}_{\phi(p)} \subset \mathbb{R}^n : \mathbf{v} \mapsto \phi_*(\mathbf{v}) = J_\phi \mathbf{v}, \tag{3.3}$$

where J_ϕ is the Jacobian matrix of map ϕ between the manifolds.

3.1.3 Metric tensor

If line segments are pushed forward to other coordinate charts, they can be squished together or stretched out. Meanwhile, it is still the same line segment so its length should not change. A notion of length is created by the metric tensor. The metric tensor is given by:

$$g_{ij} = \langle \mathbf{e}_i, \mathbf{e}_j \rangle \qquad i, j = 1, 2, ..., n \tag{3.4}$$

where $\langle \cdot, \cdot \rangle : \mathrm{TM}_p \times \mathrm{TM}_p \to \mathbb{R}^+$ is the inner product operator and $\mathbf{e}_i$ are the basis vectors of the coordinate chart. The metric tensor output is dependent on the sizes of and the angle between the basis vectors. For example, the metric tensor in matrix form for two-dimensional Cartesian coordinates is given by:

$$g_{ij} = \begin{pmatrix} 1 & 0 \\ 0 & 1 \end{pmatrix}. \tag{3.5}$$

The inverse of the metric tensor is denoted by g^{ij}. Contraction between the metric tensor and its inverse gives the Kronecker delta ($g_{ik}g^{kj} = \delta^i_j$).

The length of unit vectors are often called Lamé coefficients [7]. The Lamé coefficients H_i are given by

$$(H_i)^2 = g_{ii} = \langle \mathbf{e}_i, \mathbf{e}_i \rangle \qquad (i = 1, 2, ..., n). \tag{3.6}$$

To determine the length of a vector, solely the components of a vector is not enough. The length of the basis vectors is also of importance. Therefore, the Lamé coefficients are used to determine the length of vectors [8]. Take for example the length of vector $\mathbf{v}$ in basis $\{\mathbf{e}_i\}_{i=1,2,\dots,n}$. Vector $\mathbf{v}$ is given by the contraction of the vector components with the basis vectors:

$$\mathbf{v} = v^i \mathbf{e}_i = H_i v^i \frac{\mathbf{e}_i}{H_i} \tag{3.7}$$

where v^i are the components of vector $\mathbf{v}$ relative to the given basis. The division by H_i ensures that $\frac{\mathbf{e}_i}{H_i}$ has length 1. Therefore the magnitude of $\mathbf{v}$ is

$$|\mathbf{v}| = \sqrt{H_i^2 (v^i)^2}. \tag{3.8}$$

3.1.4 Covariant derivative

In pedestrian dynamics velocities, and therewith the derivative operator ($\frac{\partial}{\partial x}$), play an important role. The ordinary derivative operator can be used on flat manifolds. In this context, flat means that vectors do not change over the manifold. The Cartesian coordinates are an example of this. The basis vector $\mathbf{e}_x$ is for example the same everywhere in $\mathbb{R}^2$. In curved space, on the other hand, the magnitude and direction of basis vectors vary over the space. Since the ordinary derivative operator does not work in curved space, another derivative operator is needed that corrects for the changing basis vectors. This operator is called the covariant derivative. The covariant derivative of vector $\mathbf{u}$ in the direction of $\mathbf{v}$ is given by:

$$\nabla_{\mathbf{v}}\mathbf{u} = \frac{\partial \mathbf{u}}{\partial \mathbf{v}} + u^k u^j \Gamma^i_{kj}\mathbf{e}_i, \tag{3.9}$$

Where Γ^i_{kj} are called connection coefficients or *Christoffel symbols of the second kind.* As can be seen in this equation, the covariant derivative consists of two parts. The first part ($\frac{\partial \mathbf{u}}{\partial \mathbf{v}}$) is the ordinary derivative of vector $\mathbf{u}$ in the direction of $\mathbf{v}$. The second part is a correction term that takes the change of basis vectors into account. The Christoffel symbols are determined by

$$\nabla_{\mathbf{e}_j}\mathbf{e}_i = \Gamma^k_{ij}\mathbf{e}_k. \tag{3.10}$$

This equation shows that if basis vector $\mathbf{e}_i$ is transported in the direction $\mathbf{e}_j$, the change of basic vector $\mathbf{e}_i$ is given by the vector $\Gamma^k_{ij}\mathbf{e}_k$. The Christoffel symbols are not uniquely defined. The alternative name *connection coefficients* suggests that Christoffel symbols determine how different tangent spaces are connected on a manifold. By defining the way Christoffel symbols are calculated, the connection is defined. The most common connection is the Levi-Civita connection. This connection computes the Christoffel symbols by

$$\Gamma^k_{ij} = \frac{1}{2} g^{k\ell}\left(\partial_i g_{\ell j} + \partial_j g_{\ell i} - \partial_\ell g_{ij}\right). \tag{3.11}$$

The Levi-Civita connection is also the connection that is used in this thesis until further notice. From Equation (3.10) and (3.11), it follows that the Christoffel symbols are equal to 0 for flat space. As a consequence, the covariant derivative acts like an ordinary derivative in flat space.

The covariant derivative can also be pushed forward to other coordinate charts. This push-forward induces a relation between Christoffel symbols in different coordinate charts given by

$$\Gamma^k_{ij} = T^k_\ell\left(S^m_j S^n_i \overline{\Gamma}^\ell_{nm} + \partial_j S^\ell_i\right), \tag{3.12}$$

where $T = J_\phi$, $S = J_{\phi^{-1}} = [J_\phi]^{-1}$, $\phi : \Omega_\alpha \to \Omega_\beta$ and Γ^k_{ij} and $\overline{\Gamma}^k_{ij}$ the Christoffel symbols in the coordinate charts ϕ_α and ϕ_β respectively.

3.1.5 Parallel transport and Geodesics

The covariant derivative can be used when it comes to transporting over a manifold. Suppose vector $\mathbf{u}$ is transported over a manifold in the direction of $\mathbf{v}$ from tangent space to tangent space. The tangent spaces are connected via the Levi-Civita connection. A covariant derivative equal to 0 means that vector $\mathbf{u}$ does not change when it is observed in each tangent space. This concept is also called parallel transport. The parallel transport of vector $\mathbf{u}$ in the direction of $\mathbf{v}$ is given by:

$$\nabla_{\mathbf{v}}\mathbf{u} = 0. \tag{3.13}$$

Suppose that $\mathbf{u}$ is a velocity vector. If this velocity vector is transported parallel in its own direction, the velocity vector does not change. This means the motion has no acceleration and is therefore force-free. In Chapter 2, force-free motions resulted in straight paths. However, if the concept of parallel transport is used in curved space, the resulted path is not necessarily straight. The resulted path is called a geodesic.

For a clear visualization a comparison can be made: Suppose a person starts walking straight ahead in a hilly area. The trajectory of the person looks straight until he encounters a mountain. The trajectory will be curved over the mountain. The trajectory of this person is not a straight path but it is a geodesic: the 'straightest' path.

From Equation (3.13), a differential equation could be made. If $\dot{\mathbf{x}}$ is the velocity vector, the covariant derivative in its own direction is given by:

$$\nabla_{\dot{x}}\dot{x} = (\ddot{x}^k + \Gamma^k_{ij}\dot{x}^i\dot{x}^j)e_k = \vec{0} \implies \ddot{x}^k + \Gamma^k_{ij}\dot{x}^i\dot{x}^j = 0. \tag{3.14}$$

Since $k = 0, 1, ..., n$ the latter equation is a system of n differential equations. This system is also called the geodesic equations.

3.1.6 Example Polar Coordinates

In this subsection, the previous explained concepts will be applied to polar coordinates to improve the understanding of the theory.

Suppose a flat space ($\mathbb{R}^2$) with the Cartesian coordinate chart and the polar coordinate chart. This means that $\mathbb{R}^2$ is parametrized by Cartesian coordinates ($(x^1, x^2) = (x, y) \in \mathbb{R}^2$ with basis $\{\mathbf{e}_x, \mathbf{e}_y\}$) and polar coordinates ($(q^1, q^2) = (r, \theta) \in \mathbb{R}^2$ with basis $\{\hat{\mathbf{e}}_r, \hat{\mathbf{e}}_\theta\}$) respectively. The coordinate transformation $\phi : x \to q$ between these coordinate charts is given by

$$\phi : \begin{cases} x = r\cos\theta \\ y = r\sin\theta \end{cases} \tag{3.15}$$

and its corresponding inverse $\phi^{-1} : q \to x$ by

$$\phi^{-1} : \begin{cases} r = \sqrt{x^2 + y^2} \\ \theta = \arctan \frac{y}{x} \end{cases} . \tag{3.16}$$

Not all coordinate lines of the polar coordinates are straight and therefore this is a curvilinear coordinate system. Suppose that a straight line is now defined as a line that looks straight in the Cartesian coordinate chart. Since this chart is the most customary, this is the accustomed definition of a straight line.

The basis vectors of the polar coordinates ($\hat{\mathbf{e}}_r$ and $\hat{\mathbf{e}}_\theta$) can be expressed in the Cartesian coordinate basis vectors by

$$\hat{\mathbf{e}}_r = \frac{\partial x^i}{\partial r}\mathbf{e}_i = \cos(\theta)\mathbf{e}_x + \sin(\theta)\mathbf{e}_y, \tag{3.17}$$

$$\hat{\mathbf{e}}_\theta = \frac{\partial x^i}{\partial \theta}\mathbf{e}_i = -r\sin(\theta)\mathbf{e}_x + r\cos(\theta)\mathbf{e}_y. \tag{3.18}$$

Because of the definition of a straight line, the basis vectors in Cartesian coordinates do not vary in length over the chart. Therefore, the metric in Cartesian coordinates is given by $g_{ij} = \langle \mathbf{e}_i, \mathbf{e}_j \rangle = \delta_{ij}$. With this metric tensor and Equations (3.17) and (3.18), the metric for polar coordinates can be calculated:

$$\hat{g}_{ij} = \langle \hat{\mathbf{e}}_i, \hat{\mathbf{e}}_j \rangle = \begin{bmatrix} 1 & 0 \\ 0 & r^2 \end{bmatrix}. \tag{3.19}$$

Another result of the way straight lines were defined are the Christoffel symbols. Because the metric and the basis vectors in Cartesian parametrization do not depend on the position, the Christoffel symbols are equal to 0. Equation (3.11) confirms this. The Christoffel symbols in polar coordinates can be calculated with Equation (3.11) or (3.12). The resulted non-zero Christoffel symbols are $\overline{\Gamma}^r_{\theta\theta} = -r$, $\overline{\Gamma}^\theta_{r\theta} = \overline{\Gamma}^\theta_{\theta r} = \frac{1}{r}$.

Now the Christoffel symbols are known, the geodesic equation (Equation (3.14)) can be derived. The geodesic equation in Cartesian coordinates is simply given by:

$$\ddot{x} = 0 \wedge \ddot{y} = 0. \tag{3.20}$$

This clearly is the equation of a straight line. The geodesic equation in polar coordinates is given by:

$$\ddot{r} - r\dot{\theta}^2 = 0 \wedge \ddot{\theta} + \frac{2\dot{\theta}\dot{r}}{r} = 0. \tag{3.21}$$

Solutions of Equation (3.21) clearly do not look straight when observed in the polar coordinate chart. In Cartesian coordinates however, they look straight.

More interesting is the case where straight lines are defined to be force free motions in the polar coordinate chart instead of the Cartesian chart. This means, straight lines are redefined to be lines that look straight in the polar coordinate chart (Figure 2.2b). As a consequence, the magnitude of the polar coordinate basis vectors are the same everywhere in $\mathbb{R}^2$ and the metric tensor in this chart is given by $\hat{g}_{ij} = \delta_{ij}$. The Christoffel symbols in coordinates are equal to 0. The Christoffel symbols in the Cartesian chart can be calculated with Equation (3.12) and are given by:

$$\Gamma^x_{ij} = \begin{bmatrix} \frac{-xy^2}{r^4} & \frac{-y^3}{r^4} \\ \frac{-y^3}{r^4} & \frac{x^3+2xy^2}{r^4} \end{bmatrix} \qquad \text{and} \qquad \Gamma^y_{ij} = \begin{bmatrix} \frac{2x^2y+y^3}{r^4} & \frac{-x^3}{r^4} \\ \frac{-x^3}{r^4} & \frac{-x^2y}{r^4} \end{bmatrix}. \tag{3.22}$$

The corresponding geodesic equation is given by:

$$\begin{cases} \ddot{x} - \frac{xy^2}{r^4}\dot{x}^2 - \frac{2y^3}{r^4}\dot{x}\dot{y} + \frac{x^3+2xy^2}{r^4}\dot{y}^2 = 0 \\ \ddot{y} + \frac{2x^2y+y^3}{r^4}\dot{x}^2 - \frac{2x^3}{r^4}\dot{x}\dot{y} - \frac{x^2y}{r^4}\dot{y}^2 = 0 \end{cases}. \tag{3.23}$$

Solutions of this equations are straight lines. However, the solutions do not look straight in Cartesian coordinates (Figure 2.2a).

The geodesic equation is of high importance because its solutions are straight lines. Tools as the covariant derivative, Christoffel symbols, metric tensor and pull-back/push-forward are needed to move the geodesic equation to different coordinate charts.

3.2 Tubular neighborhood

Suppose a smooth curve in $\mathbb{R}^n$, $\gamma : [s_0, s_1] \to \mathbb{R}^n : s \mapsto \gamma(s)$, where $\gamma(s)$ are the Cartesian coordinates of the curve, $s_0, s_1 \in \mathbb{R}$ and $s \in [s_0, s_1] \subset \mathbb{R}$ the parameter of the curve. A tubular hyperspace $\mathbf{X}_h$ is the collection of points that are at a distance h from curve γ [9]. The region inside $\mathbf{X}_h$ is called the tubular neighborhood of γ with radius h. In $\mathbb{R}^3$, this looks like a circle that follows a curve (Figure 3.1a).

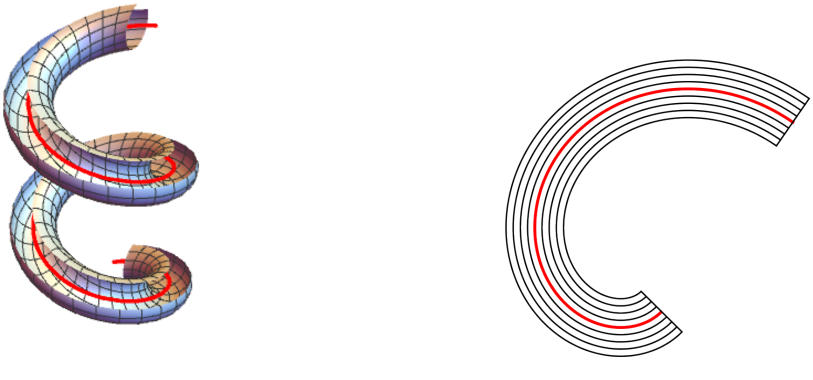

(a) **(b)**

Figure 3.1: A tubular surface around a curve in $\mathbb{R}^3$ (a) and a collection of curves parallel to the bold curve (b).

From this point on, only the two dimensional case will be considered since the pedestrian motions in this thesis will be two dimensional. In $\mathbb{R}^2$, $\mathbf{X}_h$ is also a curve at distance h from γ. In Figure 3.1b, several tubular hyperspaces are displayed that are parallel to the bold curve.

3.2.1 Coordinate frame

A coordinate chart, ϕ_γ, can be made that covers the tubular neighbourhood of a curve where the tubular hyperspaces will form coordinate lines. Since the hyperspaces are all parallel to curve γ, the first basis vector, $\mathbf{T}$, is a tangent vector of the curve:

$$\mathbf{T} = \frac{\boldsymbol{\gamma}'(s)}{|\boldsymbol{\gamma}'(s)|}, \tag{3.24}$$

where the prime ($'$) denotes the derivative with respect to s. The division by $|\gamma'(s)|$ ensures that $\mathbf{T}$ has unit length. This tangent vector is dependent on s. Therefore $\mathbf{T} = \mathbf{T}(s)$.

The other basis vector, $\mathbf{N}$, is normal to $\mathbf{T}$ and curve γ:

$$\mathbf{N} = \begin{pmatrix} \mathrm{T}^2 \\ -\mathrm{T}^1 \end{pmatrix}, \tag{3.25}$$

where T^i denote the components of $\mathbf{T}$. This normal vector is obtained by a clockwise rotation of the tangent vector by $\frac{\pi}{2}$ radians. Vector $\mathbf{N} = \mathbf{N}(s)$ can describe the tubular hyperspace $\mathbf{X}_h$ as follows:

$$\mathbf{X}_h(s) = \boldsymbol{\gamma}(s) + h\mathbf{N}(s). \tag{3.26}$$

The latter formula can only describe tubular hyperspaces $\mathbf{X}_h$ for $|h|$ not too large. Figure 3.2 shows an example of a curve with a tubular hyperspace $\mathbf{X}_h$ where $|h|$ is too large. Because of the curvature of the ellipse, the parallel curve intersects itself. The curvature k and radius of curvature R are given by [7]

$$k(s) = \frac{\gamma_x'(s)\gamma_y''(s) - \gamma_x''(s)\gamma_y'(s)}{[(\gamma_x'(s))^2 + (\gamma_y'(s))^2]^{3/2}}, \qquad R(s) = \frac{1}{k(s)}, \tag{3.27}$$

where γ_x and γ_y are the x and y component of γ respectively. A safe upper bound for $|h|$ is the minimal radius of curvature:

$$|h| < h_{\max} = \min_{s\in[s_0,s_1]} R(s). \tag{3.28}$$

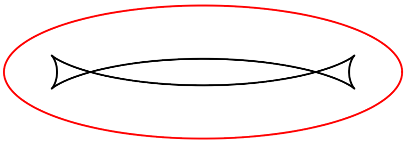

Figure 3.2: An ellipse with a curve parallel to it ($\mathbf{X}_h$). The curve $\mathbf{X}_h$ intersects itself since $|h|$ is too large.

Coordinate chart $\phi_\gamma : \Omega_\gamma \to \mathbb{R}^2$ covers the region Ω_γ between $\mathbf{X}_{-h_{\max}}$ and $\mathbf{X}_{h_{\max}}$. The coordinates of ϕ_γ are $(s^1, s^2) = (s, h)$. Coordinate h indicates on which parallel curve $\mathbf{X}_h$ a point lies. The other coordinate, s, is the parameter of the curve and indicates how far on $\mathbf{X}_h(s)$ the point lies.

3.2.2 Coordinate transformation

A coordinate transformation ϕ exists between coordinate chart ϕ_γ and the Cartesian coordinate chart in the region Ω_γ. Map $\phi : \phi_\gamma(\Omega_\gamma) \to \phi_x(\Omega_\gamma) : s \mapsto x = \phi(s)$, where ϕ_x represents the Cartesian coordinate chart and $x, s \in \mathbb{R}^2$ are coordinates in charts ϕ_x and ϕ_γ respectively, is given by:

$$\phi(s, h) = \mathbf{X}_h(s) = \boldsymbol{\gamma}(s) + h\mathbf{N}(s). \tag{3.29}$$

3.2.3 Pull-back

With the coordinate transformation in Equation (3.29) points and vectors can be pushed forward from chart ϕ_γ to the Cartesian chart. For a pull-back, the inverse mapping ϕ^{-1} is needed. However, it is not always possible to derive an expression for ϕ^{-1}. The Newton-Raphson method will help with an approximate but accurate pull-back.

Newton-Raphson method

The two dimensional Newton-Raphson method is an iterative method for solving solutions in the form $\mathbf{f}(\mathbf{x}) = 0$. If $\mathbf{x}_0$ is an approximate solution, then the sequence

$$\mathbf{x}_{p+1} = \mathbf{x}_p - J^{-1}(\mathbf{x}_p)\mathbf{f}(\mathbf{x}_p) \qquad p = 1, 2, ... \tag{3.30}$$

converges to a solution of $\mathbf{f}(\mathbf{x}) = 0$ [10]. In Equation (3.30), J^{-1} represents the Jacobian of $\mathbf{f}$ with respect to $\mathbf{x}$.

In the case that this method is used to pull-back a known point ($\hat{x}$) from the Cartesian coordinate chart to chart ϕ_γ, function $\mathbf{f}$ is given by

$$\mathbf{f} = \phi(s) - \hat{x}. \tag{3.31}$$

The Newton-Raphson approximates the roots of $\mathbf{f}$ and therewith solutions of $\phi(s) = \hat{x}$ where $s = \phi^{-1}(\hat{x})$.

The Newton-Raphson method has quadratic convergence [11] which means

$$|\hat{s} - s_{n+1}| \sim |\hat{s} - s_n|^2 \tag{3.32}$$

where $\hat{s}$ is a root of $\mathbf{f}$ and s_n the approximation of root $\hat{s}$.

3.3 Stochastic differential equations

The geodesic equation (Equation (3.14)) form the base of the model for fluctuating pedestrian dynamics. In order to simulate trajectories of pedestrians, the geodesic equation has to be solved. In $\mathbb{R}^2$, this is a system of four ordinary differential equations (ODE). Several modeling forces will be added to this equation to, among other things, take the stochastic behaviour of pedestrians into account. The stochastic terms that these modeling forces contain, cause the system of ODE's to become a system of stochastic differential equations (SDE). The required knowledge about stochastic differential equations will be discussed in this chapter.

3.3.1 Brownian motion

A Brownian motion is a continuous stochastic process W with the following properties [12]:

i $W(0) = 0$;

ii $W(t) - W(s) \sim \mathcal{N}(0, t - s)$, for any $0 \leq s < t$;

iii $W(t_1) - W(t_0), W(t_2) - W(t_1), \cdots, W(t_k) - W(t_{k-1})$ are independent random variables for each $k \geq 2$ and $0 = t_0 < t_1 < \cdots < t_k$.

For a two-dimensional stochastic process, $\mathbf{W}(t)$, to be a two-dimensional Brownian motion, both components, $W_1(t)$ and $W_2(t)$, should be independent one-dimensional Brownian motions.

3.3.2 Construction of an SDE

Let $x(t)$ be a function satisfying the following ordinary differential equation:

$$\frac{dx(t)}{dt} = a(t, x(t)) \tag{3.33}$$

with initial value $x(0) = x_0$ and $a(t, x(t))$ an arbitrary function. This differential equation has the following solution:

$$x(t) = x_0 + \int_0^t a(\tau, x(\tau))d\tau. \tag{3.34}$$

Suppose that $a(t, x(t))$ is now a continuous stochastic process of the following form:

$$a(t, X(t)) = f(t, X(t)) + g(t, X(t))\eta(t), \tag{3.35}$$

where f and g are arbitrary functions and η is Gaussian white noise. This means that $\eta(t) \sim \mathcal{N}(0, 1)$ for all t. Note that function x is now a random variable X. The ODE in Equation (3.33) transforms in a stochastic differential equation given by

$$\frac{dX(t)}{dt} = f(t, X(t)) + g(t, X(t))\eta(t). \tag{3.36}$$

The Gaussian noise term is regarded as the derivative of a Brownian motion ($\eta(t) = \dot{W}(t)$) [13]. The stochastic differential equation can be written as

$$\frac{dX(t)}{dt} = f(t, X(t)) + g(t, X(t))\dot{W}(t). \tag{3.37}$$

A solution of this SDE is given by

$$X(t) = X_0 + \int_0^t f(\tau, X(\tau))d\tau + \int_0^t g(\tau, X(\tau))dW(\tau), \tag{3.38}$$

where $X_0 = X(0)$.

The two integrals in this equation are supposed to be well defined. The latter integral is referred to as an Itô integral.

3.3.3 Numerical method for approximating SDE's

Suppose the stochastic differential equation

$$dX(t) = f(t, X(t))dt + g(t, X(t))dW(t), \quad X(0) = X^{(0)} \tag{3.39}$$

where $X(t)$, $f(t, X(t))$ and $g(t, X(t))$ are n-dimensional vectors, $g(t, X(t))$ is a $n \times n$-matrix and $W(t)$ a n-dimensional Brownian motion. This can also be written as

$$dX_i(t) = f_i(t, X(t))dt + \sum_{k=1}^{n} g_{ik}(t, X(t))dW_k(t), \quad X_i(0) = X_i^{(0)} \tag{3.40}$$

where $i = 1, 2, \cdots, n$. For the approximation of the solution, the interval $[0, T]$ is divided into N equal intervals with length $h = T/N$.

A simple numerical method for approximating the solution of stochastic differential equations is the Euler-Maruyama scheme [14]. The Euler-Maruyama scheme is given by

$$x_i^{(j+1)} = x_i^{(j)} + f_i\left(jh, x^{(j)}\right)h + \sum_{k=1}^{n} g_{ik}\left(jh, x^{(j)}\right)\Delta W_k^{(j)}, \tag{3.41}$$

where $\Delta W_k^{(j)} = W_k((j+1)h) - W_k(jh)$ and $x^{(j)}$ represents the numerical approximation of $X(jh)$. Note that $0 \leq j \leq N$.

The Euler-Maruyama method is has a strong order convergence of 0.5. Although this method is very efficient, more accurate methods exist. The stochastic Runge-kutta (SRK) method, for example, has strong order of convergence 1.0 [15].

4. Model

In this section, the mathematical model will be constructed step by step. The goal is to model diluted pedestrian dynamics fluctuating around curved paths. First a relatively simple model will be used to model force-free pedestrian dynamics on circular paths. Then, generic curved paths will be considered. After this, the modeling forces (lateral confinement, longitudinal propulsion and white noise) based on the discussed model for fluctuating pedestrian dynamics around straight paths (Chapter 2, [4]) will be introduced. The modeling forces will be added to create a realistic model for fluctuating pedestrian dynamics.

4.1 Force free equations

To begin, motions of pedestrians will be considered where no forces are present. The path that a pedestrian desires to follow is referred to as base-path. Since pedestrians follow geodesics when moving in a force-free environment, the base-path and parallel paths need to be a geodesics. As explained in the conceptual framework, Chapter 2, pedestrians are compared with particles governed by Newtonian dynamics. The Cartesian coordinate system best resembles the physical space concerning velocities and length. Therefore the particles are considered to move in the Cartesian representation of $\mathbb{R}^2$.

4.1.1 Example circular trajectories

Suppose pedestrians desire to follow a circular path. Then, a circular base-path is demanded to be a geodesic. In order to define a circle to be a geodesic in a simple way, the coordinate chart has to be found where it looks like a straight line. Then, straight lines can be redefined to resemble force-free motions in this coordinate chart. Luckily, circles are not complex trajectories. The suitable coordinate chart is already known: the polar coordinate chart. The example of the polar coordinates has already been elaborated in Section 3.1.6. In the explained setting, the geodesic equation in Cartesian coordinates is given in Equation (3.23). In Figure 4.1, examples of solutions of the geodesic equation can be seen in polar coordinates as well as Cartesian coordinates. Also, the velocity plot is shown for each solution.

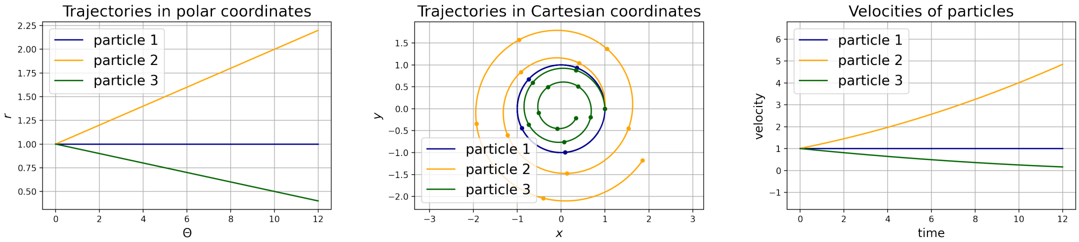

(a) **(b)** **(c)**

Figure 4.1: Examples of trajectories along geodesics in polar coordinates (a), in Cartesian coordinates (b) and the corresponding velocity magnitudes (c).

The different trajectories in Figure 4.1b are the result of different initial conditions of the particles. The particles that follow a spiral in Figure 4.1b do not follow a circle. However, these trajectories are still geodesics because they resemble straight lines in the polar coordinate chart (Figure 4.1a).

In Figure 4.1c, the magnitudes of the velocity of each particle can be seen. The particle that follows the circle has a constant velocity. The particles that follow a spiral on the other hand, are accelerating or decelerating. Take for example the outwards spiraling 'particle 2'. This particle constantly moves to a greater circle but keeps the angular velocity constant. Because a greater circle covers more distance and the particle covers that distance in the same amount of time, the particle has to accelerate. Likewise, 'particle 3' is decelerating.

4.1.2 Energy conservation

From the pedestrian point of view, it does not make sense to accelerate when a straight path is followed in a force-free environment. Perturbations from a curved base-path should not lead to accelerations. To keep energy and velocity conserved another connection has to be chosen. That means that the Levi-Civita connection (Equation (3.11)) is no longer valid and another way of determining the Christoffel symbols is needed.

The circular geodesic equation in polar coordinates endowed with the Levi-Civita connection is given by:

$$\begin{cases} \ddot{r} = 0 \\ \ddot{\theta} = 0 \end{cases} . \tag{4.1}$$

As mentioned before, the Cartesian coordinate chart is the coordinate chart that best resembles the physical space. Therefore, velocities and line segments should be observed in the Cartesian chart. For the definition of geodesics, the metric in polar coordinates was defined to be $\hat{g}_{ij} = \delta_{ij}$. However, when it comes to measuring the length of vectors the Lamé coefficients are used with respect to a Cartesian metric of $g_{ij} = \delta_{ij}$. The Lamé coefficients (Equation (3.6)) in the polar coordinate chart are given by:

$$H_r = 1 \qquad \text{and} \qquad H_\theta = r \tag{4.2}$$

The resulting length of velocity vector $\mathbf{v} = (\dot{r}, \dot{\theta})$ is $|\mathbf{v}|^2 = \dot{r}^2 + (r\dot{\theta})^2$ which is a result of Equation (3.8). The physical velocity component in the angular direction is thus given by $r\dot{\theta}$. For energy conservation the physical velocity component ($r\dot{\theta}$, unit [ms^{-1}]) should be conserved instead of the angular velocity ($\dot{\theta}$, unit [s^{-1}]). The geodesic equation (Equation (4.1)) evolves in:

$$\begin{cases} \ddot{r} = 0 \\ \frac{d}{dt}(r\dot{\theta}) = r\ddot{\theta} + \dot{r}\dot{\theta} = 0 \implies \ddot{\theta} + \frac{1}{r}\dot{r}\dot{\theta} = 0 \end{cases} . \tag{4.3}$$

Equation (3.14) shows how the Christoffel symbols play a role in the geodesic equation. The obtained Christoffel symbols from Equation (4.3) are $\overline{\Gamma}^{\theta}_{r\theta} = \overline{\Gamma}^{\theta}_{\theta r} = \frac{1}{2r}$. The push-forward of these Christoffel symbols (Equation (3.12)) are given by

$$\Gamma^x_{ij} = \begin{bmatrix} 0 & -\frac{y}{2r^2} \\ -\frac{y}{2r^2} & \frac{x}{r^2} \end{bmatrix} \qquad \text{and} \qquad \Gamma^y_{ij} = \begin{bmatrix} \frac{y}{r^2} & -\frac{x}{2r^2} \\ -\frac{x}{2r^2} & 0 \end{bmatrix} \tag{4.4}$$

and the corresponding geodesic equation by

$$\begin{cases} \ddot{x} = \frac{y}{r^2}\dot{x}\dot{y} - \frac{x}{r^2}\dot{y}^2 \\ \ddot{y} = -\frac{y}{r^2}\dot{x}^2 + \frac{x}{r^2}\dot{x}\dot{y} \end{cases} . \tag{4.5}$$

In Figure 4.2, three trajectories of particles are shown in polar coordinates and Cartesian coordinates. The particles in this figure have the same initial conditions (i.e. starting position and velocity) as the particles in Figure 4.1. The velocity plot (Figure 4.2c) shows that the magnitude of the velocity and therewith the energy is now conserved. Also in Figure 4.2b, it can be seen that 'particle 2' that spirals outwards does not accelerate anymore the way it did as it makes less rotations in the same amount of time.

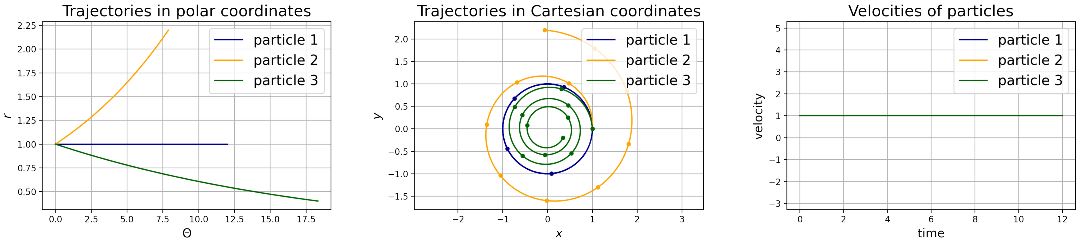

(a) **(b)** **(c)**

Figure 4.2: Examples of trajectories along geodesics in polar coordinates (a), in Cartesian coordinates (b) and the corresponding velocity magnitudes (c).

4.1.3 Generic curves

The coordinate chart that makes circles in the Cartesian chart look like straight lines is well-known (Section 3.1.6). In a similar fashion, elliptical coordinates can be used to let a ellipse look a straight line, as will be continued in Chapter 6. But what if the desired path is a randomly curved path?

Take a generic curve γ that serves as base-path. As explained in Section 3.2.1, coordinate chart ϕ_γ has coordinate lines that are parallel to curve γ. That makes chart ϕ_γ a good candidate to use for the definition of geodesics. The basis vectors of chart ϕ_γ are the tangent and normal vectors of curve γ and the coordinates s and h represent the progression over the curve and the distance from the curve respectively. The basis vectors can be obtained from Equations (3.24) and (3.25) and the coordinate transformation between the Cartesian coordinates and the coordinate chart ϕ_γ from Equation (3.29).

For example, let γ be the parabola-shaped curve given by:

$$\gamma(s) = (s, s^2) \qquad -2 \leq s \leq 2. \tag{4.6}$$

The corresponding basis vectors for ϕ_γ are given by:

$$\mathbf{T}(s) = \frac{1}{\sqrt{4s^2+1}}\begin{pmatrix}1\\2s\end{pmatrix} \qquad \text{and} \qquad \mathbf{N}(s) = \frac{1}{\sqrt{4s^2+1}}\begin{pmatrix}2s\\-1\end{pmatrix}. \tag{4.7}$$

The coordinate transformation ϕ is given by:

$$\phi(s,h) : \begin{cases} x = \frac{2hs}{\sqrt{4s^2+1}} + s \\ y = -\frac{h}{\sqrt{4s^2+1}} + s^2 \end{cases}. \tag{4.8}$$

The minimal radius of curvature of the parabola is $1/2$ which is achieved at the bottom of the parabola. Therefore coordinate h is in the interval $[-\frac{1}{2}, \frac{1}{2}]$. In Figure 4.3, the curve is shown in the Cartesian coordinate chart as well as the chart ϕ_γ. A (s,h) coordinate frame is also plotted in the Cartesian coordinates. It is clearly visible that the tangent vectors and normal vectors form the basis vectors of the (s,h)-parametrization.

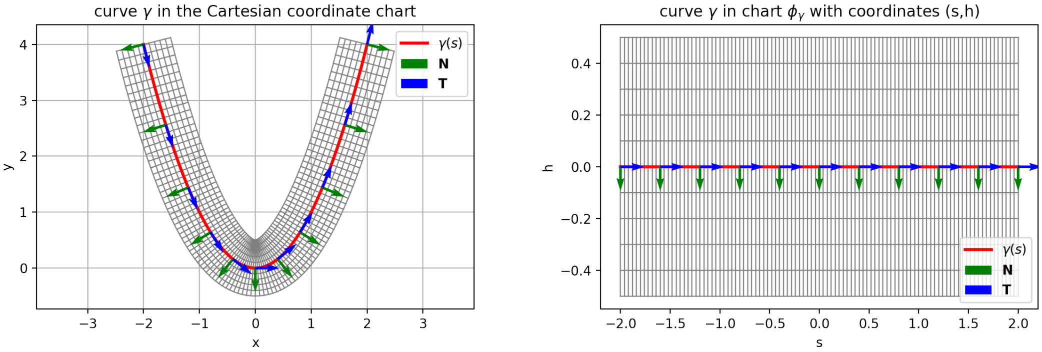

(a) **(b)**

Figure 4.3: Parabola-shaped curve γ in the Cartesian coordinate chart (a) and in chart ϕ_γ (b). Normal (**N**) and tangent vectors (**T**) are displayed at several points on the curve.

The curve γ can be defined to be a geodesic. This is done similarly as it was done in the circular trajectory example. The Christoffel symbols in coordinate chart ϕ_γ ($\overline{\Gamma}^k_{ij}$) are defined to be equal to 0: $\overline{\Gamma}^k_{ij} = 0$. The Christoffel symbols can be pushed-forward to the Cartesian chart with Equation (3.12). The Christoffel symbols in the Cartesian chart are denoted by Γ^k_{ij}.

The geodesic equation in chart ϕ_γ is given by:

$$\begin{cases} \ddot{s} = 0 \\ \ddot{h} = 0 \end{cases} . \tag{4.9}$$

Two solutions of geodesic Equation (4.9) with different initial conditions are shown in Figure 4.4. In Figure 4.4b, it can clearly be seen that the two trajectories look like straight lines in chart ϕ_γ. The velocity plot in Figure 4.4c shows that Equation (4.9) does not conserve energy. The same problem was encountered in the polar coordinates example. Instead of conserving the coordinate velocity ($\ddot{s} = 0 \wedge \ddot{h} = 0$), the physical velocity components should be conserved:

$$\frac{\mathrm{d}}{\mathrm{d}t}(H_s \dot{s}) = 0 \wedge \frac{\mathrm{d}}{\mathrm{d}t}(H_h \dot{h}) = 0. \tag{4.10}$$

In order to calculate the Lamé coefficients, first the coordinate transformation ϕ is rewritten as

$$\phi(s,h) : \begin{cases} \phi_x(s,h) = \gamma_x(s) + hN_x(s) \\ \phi_y(s,h) = \gamma_y(s) + hN_y(s) \end{cases} , \tag{4.11}$$

in which N_x and N_y are the x and y components of $\mathbf{N}$ respectively. The Jacobian of this mapping is

$$J_\phi = \begin{pmatrix} \partial_s \phi_x & \partial_h \phi_x \\ \partial_s \phi_y & \partial_h \phi_y \end{pmatrix} = \begin{pmatrix} \gamma'_x(s) + hN'_x(s) & N_x(s) \\ \gamma'_y(s) + hN'_y(s) & N_y(s) \end{pmatrix} , \tag{4.12}$$

in which ∂_i represents the derivative with respect to i. The basis vectors of chart ϕ_γ, $\hat{\mathbf{e}}_s$ and $\hat{\mathbf{e}}_h$, can now be expressed in the Cartesian basis vectors by (Equation (3.1))

$$\hat{\mathbf{e}}_s = \frac{\partial x^i}{\partial s}\mathbf{e}_i = \partial_s \phi_x \mathbf{e}_x + \partial_s \phi_y \mathbf{e}_y, \tag{4.13}$$

$$\hat{\mathbf{e}}_h = \frac{\partial x^i}{\partial s}\mathbf{e}_i = N_x(s)\mathbf{e}_x + N_y(s)\mathbf{e}_y. \tag{4.14}$$

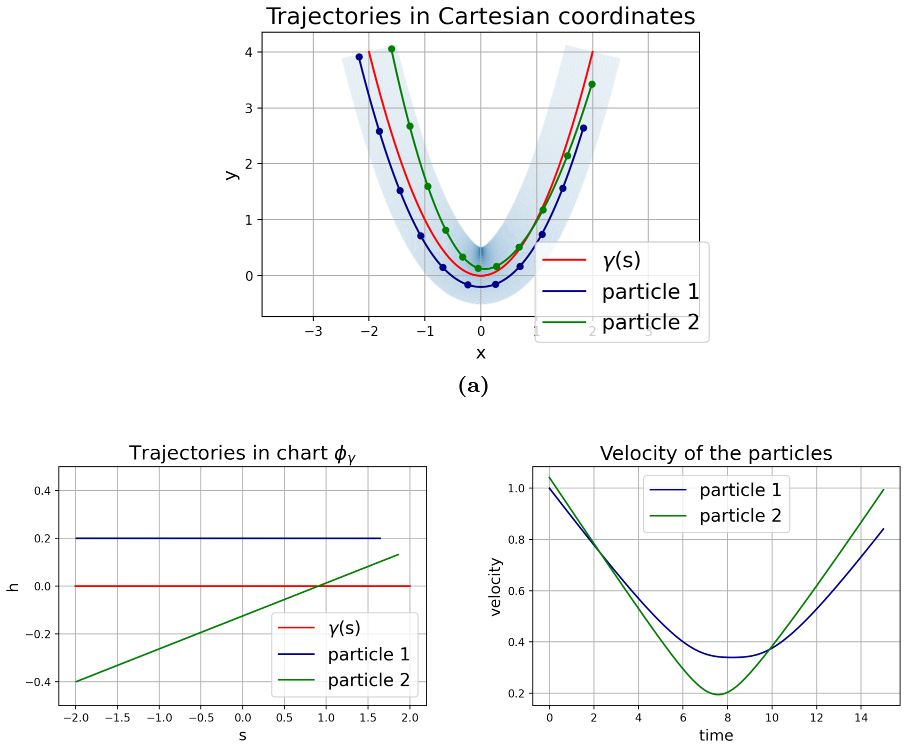

(a)

(b) **(c)**

Figure 4.4: Examples of trajectories along geodesics in Cartesian coordinates (a), in chart ϕ_γ (b) and the corresponding velocity magnitudes (c). In the Cartesian chart, the s,h-coordinate frame is plotted in light blue.

From the last equation, it can be observed that the length of $\hat{\mathbf{e}}_h$ is the same as the length of $\mathbf{N}$ which is equal to 1. The corresponding Lamé coefficient, H_h, is therefore equal to 1. With Equation (3.6), the other Lamé coefficient can be determined. The resulted Lamé coefficients are

$$H_s = \sqrt{(\partial_s\phi_x)^2 + (\partial_s\phi_y)^2} \tag{4.15}$$

$$H_h = 1. \tag{4.16}$$

The physical velocity component $H_h\dot{h} = \dot{h}$ is easily conserved with the equation $\ddot{h} = 0$. The conservation of the physical velocity component $H_s\dot{s}$ results from the expansion of $\frac{d}{dt}(H_s\dot{s}) = 0$:

$$\ddot{s} + \frac{\partial_s\phi_x(\partial_s)^2\phi_x + \partial_s\phi_y(\partial_s)^2\phi_y}{H_s^2}\dot{s}^2 + \frac{\partial_s\phi_x\partial_s\partial_h\phi_x + \partial_s\phi_y\partial_s\partial_h\phi_y}{H_s^2}\dot{s}\dot{h} = 0. \tag{4.17}$$

The Christoffel symbols can be obtained from this equation resulting in

$$\overline{\Gamma}^s_{ij} = \begin{bmatrix} \frac{\partial_s\phi_x(\partial_s)^2\phi_x+\partial_s\phi_y(\partial_s)^2\phi_y}{H_s^2} & \frac{\partial_s\phi_x\partial_s\partial_h\phi_x+\partial_s\phi_y\partial_s\partial_h\phi_y}{2H_s^2} \\ \frac{\partial_s\phi_x\partial_s\partial_h\phi_x+\partial_s\phi_y\partial_s\partial_h\phi_y}{2H_s^2} & 0 \end{bmatrix} \quad \text{and} \quad \overline{\Gamma}^h_{ij} = 0. \tag{4.18}$$

The Christoffel symbols can be pushed forward to the Cartesian chart and the geodesic equation can be derived (Equation (3.14)):

$$\begin{cases} \ddot{x} + \Gamma^x_{ij}\dot{x}^i\dot{x}^j = 0 \\ \ddot{y} + \Gamma^y_{ij}\dot{x}^i\dot{x}^j = 0 \end{cases} . \tag{4.19}$$

Because the Christoffel symbols are often complex expressions, they will simply be denoted by Γ^k_{ij}. During simulations, the Christoffel symbols are numerically determined in chart ϕ_γ with Equation

(4.18) and numerically pushed forward to the Cartesian chart with Equation (3.12). More about the simulations follows in Chapter 5.

To continue with the parabolic curve, two solution of the new geodesic equation, endowed with the energy conserving connection, with different initial conditions are shown in Figure 4.5. In Figure 4.5c, it can be seen that the velocity stays constant and hence the energy is indeed conserved.

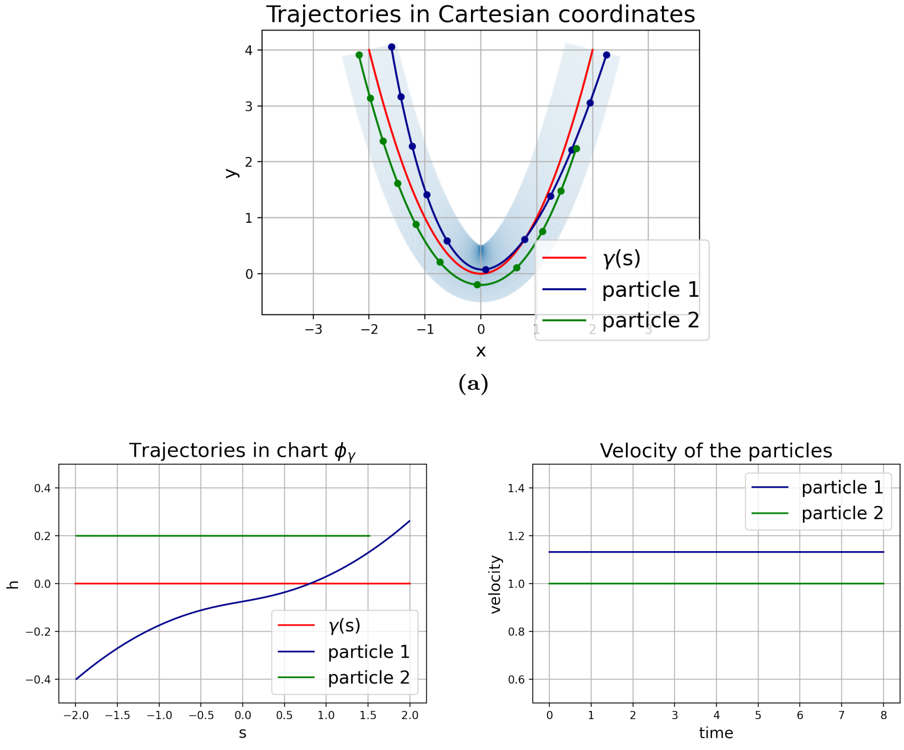

(a)

(b) **(c)**

Figure 4.5: Example of trajectories along geodesics endowed with the energy conserving connection in Cartesian coordinates (a), in chart ϕ_γ (b) and the corresponding velocity magnitudes (c). In the Cartesian chart, the s,h-coordinate frame is plotted in light blue.

4.2 Confinement potential

Now that there is a force-free model that can be used for force-free trajectories along geodesics, modeling forces should be added to let the resulting trajectories resemble real-life pedestrian trajectories. The left hand side of Equation (4.19) represents the acceleration along a geodesic. As Newton's second law suggests, the modeling forces should be added on the right hand side of Equation (4.19). The modeling forces that are added in the upcoming sections are based on the existing model for fluctuating pedestrian dynamics along straight paths [4]. This model is explained in Chapter 2 and displayed in the Equations (2.2)-(2.5).

The first modeling forces are the resulting forces of two harmonic confinement potentials. Like the model for straight paths, this is a position potential and a velocity potential. The resulting forces are working in the transversal direction (i.e. normal to the base-path). The coordinate that h in chart ϕ_γ represents the lateral distance from the base-path γ. The position potential is given by

$$\Phi_h(h) = \beta h^2 \tag{4.20}$$

in which β is a scale parameter. The resulting force is

$$-\nabla\Phi_h = -2\beta h\hat{\mathbf{e}}_h = -2\beta h N_x(s)\mathbf{e}_x - 2\beta h N_y(s)\mathbf{e}_y. \tag{4.21}$$

The transversal velocity is is given by $H_h \dot{h} = \dot{h}$. In Cartesian coordinates this velocity component is obtained by the inner product of the velocity vector in Cartesian coordinates and the unit vector normal to the curve. Let $\mathbf{u} = \begin{pmatrix} \dot{x} \\ \dot{y} \end{pmatrix} = \begin{pmatrix} u \\ v \end{pmatrix}$. Then,

$$V_\perp = \langle \mathbf{u}, \mathbf{N} \rangle = uN_x(s) + vN_y(s) \tag{4.22}$$

is the velocity in the normal direction.

The velocity potential,

$$\Phi_{V_\perp} = \mu V_\perp^2, \tag{4.23}$$

creates the following force:

$$\begin{aligned} -\nabla \Phi_{V_\perp} &= -2\mu V_\perp \hat{\mathbf{e}}_h = -2\mu V_\perp N_x(s)\mathbf{e}_x - 2\mu V_\perp N_y(s)\mathbf{e}_y \\ &= -2\mu(uN_x + vN_y) \begin{pmatrix} N_x \\ N_y \end{pmatrix}. \end{aligned} \tag{4.24}$$

The equation of motion is originated from the geodesic Equation (4.19). With the confinement potential forces included, particles would behave according to

$$\begin{cases} \dot{\mathbf{x}} = \mathbf{u} \\ \dot{\mathbf{u}} = -\Gamma^k_{ij} u^i u^j \mathbf{e}_k - \nabla \Phi_h - \nabla \Phi_{V_\perp} \end{cases}. \tag{4.25}$$

This equation is in vector notation and is a system of four ordinary differential equations.

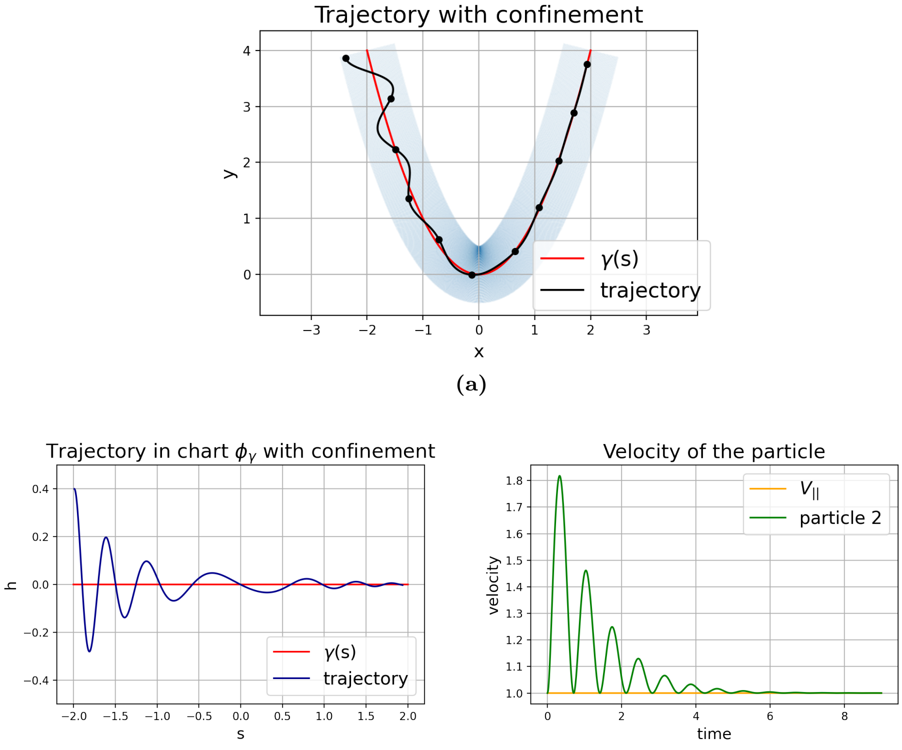

(a)

(b)

(c)

Figure 4.6: A simulated trajectory of the equation of motion with the confinement force. The scale parameters are set to $\beta = 10$ and $\mu = 0.5$. The trajectory is shown in Cartesian coordinates (a) and in chart ϕ_γ (b). The magnitude of the velocity and the velocity parallel to the curve are plotted in (c).

A solution of Equation (4.25) for the parabolic curve γ from previous section is shown in Figure 4.6. The starting position of the particle is at a lateral distance to the curve. The position potential pushes the particle to the curve which causes the particle to accelerate in the normal direction. This acceleration can be seen in Figure 4.6c. In this figure, also the longitudinal velocity, $V_{\|}$, is plotted which is the velocity parallel to the curve. It can be seen that the longitudinal velocity stays constant during the simulation so the acceleration is solely in the normal direction. The position potential causes the particle to oscillate along the curve. The velocity potential damps this oscillation.

4.3 Longitudinal propulsion

The second modeling force is a longitudinal propulsion force. The role of this force is to keep the longitudinal velocity around a desired value. When a particle propagates too fast over the desired curve, this force slows the particle down and vice versa. As a result, perturbations in the longitudinal velocity are damped.

The longitudinal propulsion force is a resulting force of a longitudinal velocity potential. This potential has a potential well centered at a preferred longitudinal velocity. The model for straight paths, has a longitudinal velocity potential with a double potential well: one well centered at a preferred velocity and the other well centered at the negative preferred velocity. In this model however, particles are considered to move in one direction only. That is why the well at the negative preferred velocity is not necessary. The harmonic longitudinal velocity potential is obtained by a second order Taylor expansion of Equation (2.7) around the preferred velocity:

$$\Phi_{V_{\|}} = 4\alpha V_p^2 (V_{\|} - V_p)^2. \tag{4.26}$$

In this equation, $V\|$ is the longitudinal velocity, V_p is a parameter that represents the preferred velocity in the longitudinal direction and α is a scale parameter. The longitudinal velocity is obtained similarly as the transversal velocity:

$$V_{\|} = \langle \mathbf{u}, \mathbf{T} \rangle = uT_x(s) + vT_y(s). \tag{4.27}$$

The resulting force of this potential is called the longitudinal propulsion force:

$$\begin{aligned} -\nabla\Phi_{V_{\|}} &= -8\alpha V_p^2 (V_{\|} - V_p)\mathbf{T} \\ &= -8\alpha V_p^2 (uT_x + vT_y - V_p) \begin{pmatrix} T_x \\ T_y \end{pmatrix}. \end{aligned} \tag{4.28}$$

The longitudinal propulsion force is included in the equation of motion as follows

$$\begin{cases} \dot{\mathbf{x}} = \mathbf{u} \\ \dot{\mathbf{u}} = -\Gamma^k_{ij} u^i u^j \mathbf{e}_k - \nabla\Phi_h - \nabla\Phi_{V_\perp} - \nabla\Phi_{V_{\|}}. \end{cases} \tag{4.29}$$

Figure 4.7a shows the trajectory of a particle that moves according to Equation (4.29) over the parabolic curve γ. The starting position is again at a lateral distance to the curve. The confinement forces cause a damped oscillation around the curve. In Figure 4.7b, it can be seen that the initial longitudinal velocity is lower than the desired longitudinal velocity. The propulsion force accelerates the particle such that its velocity converges to the desired value.

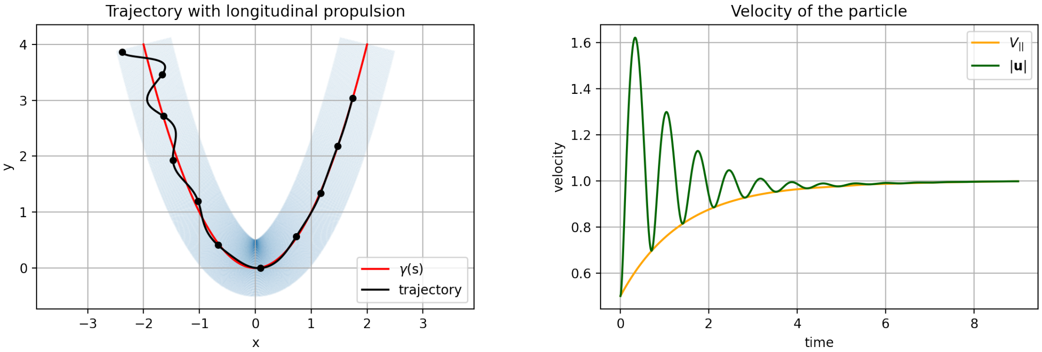

(a) **(b)**

Figure 4.7: A simulated trajectory of the equation of motion with the confinement force and longitudinal propulsion force. The scale parameters are set to $\beta = 10$, $\mu = 0.5$ and $\alpha = 0.1$ and the preferred velocity to $V_p = 1.0$. The trajectory is shown in Cartesian coordinates (a). The magnitude of the velocity and the velocity parallel to the curve are plotted in (b).

4.4 Noise

The final modeling component is a noise term. This term accounts for the stochastic velocity fluctuations that pedestrians have. The noise is considered to be Gaussian white noise which means that it is Gaussian distributed and centered at zero. The equation of motion with the noise term included is given by

$$\begin{cases} \dot{\mathbf{x}} = \mathbf{u} \\ \dot{\mathbf{u}} = -\Gamma^k_{ij} u^i u^j \mathbf{e}_k - \nabla\Phi_h - \nabla\Phi_{V_\perp} - \nabla\Phi_{V_\parallel} + \boldsymbol{\sigma}\dot{W} \end{cases} \tag{4.30}$$

where $W(t)$ is a 2-dimensional Brownian motion and $\boldsymbol{\sigma}$ is a 2×2-matrix that contains the scale parameters of the noise. Note that the derivative of a Brownian, $\dot{W}(t) = \eta(t)$, is Gaussian distributed. Assumed is that there is no correlation between the dynamics in different directions. As a result, the off-diagonal elements of $\boldsymbol{\sigma}$ are equal to 0. Furthermore, the noise is considered to be isotropic. Therefore the diagonal elements of $\boldsymbol{\sigma}$ are the same:

$$\boldsymbol{\sigma} = \begin{pmatrix} \sigma & 0 \\ 0 & \sigma \end{pmatrix}. \tag{4.31}$$

This results in the following equation of motion:

$$\begin{cases} \dot{\mathbf{x}} = \mathbf{u} \\ \dot{\mathbf{u}} = -\Gamma^k_{ij} u^i u^j \mathbf{e}_k - \nabla\Phi_h - \nabla\Phi_{V_\perp} - \nabla\Phi_{V_\parallel} + \sigma\dot{W} \end{cases} . \tag{4.32}$$

The Noise term makes the equation of motion into a to a system of four stochastic differential equations. The theory of stochastic differential equations is discussed in Section 3.3.

In Figure 4.8a, two numerical solutions of Equation (4.32) are shown. The simulation procedure is discussed in Chapter 5. The scale parameter σ for particle 1 and particle 2 are set to 0.4 and 0.1 respectively. In Figure 4.8b, it can be seen that the velocity of particle 2 has smaller fluctuations because of the lower scale parameter. The confinement force and the longitudinal propulsion force keep the velocity perturbations within bounds.

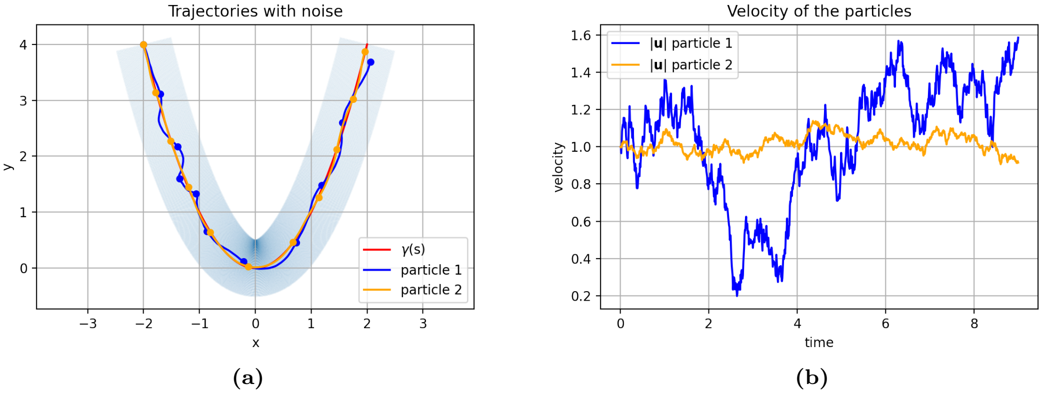

Figure 4.8: Two simulated trajectories of the equation of motion with the confinement force, the longitudinal propulsion force and the noise. The scale parameters are set to $\beta = 10$, $\mu = 0.5$ and $\alpha = 0.1$ and the preferred velocity to $V_p = 1.0$. For 'particle 1', the scale parameter for the noise is set to $\sigma = 0.4$ while this parameter for 'particle 2' is set to $\sigma = 0.1$. The trajectories are shown in Cartesian coordinates (a). The magnitude of the velocities are plotted in (b).

5. Simulations

In the proposed model (Chapter 4), the dynamics of particles behave according to Equation (4.32). Several aspects on how simulations are performed will be elaborated in this chapter.

5.1 Numerical integration method

The equation of motion (Equation (4.32)) is a system of four stochastic differential equations. Section 3.3 contains the theory about stochastic differential equations. Simulations are performed by solving the equations of motion numerically. The numerical method that is used for approximating the system of stochastic differential equations is the Runge-kutta algorithm SRI2 proposed in [15]. This method derived from the deterministic Runge-kutta for ordinary differential equations and has a strong order of convergence of 1.

The length of the discretization step during simulations is chosen to be $\frac{1}{30}$ seconds. This time step is based on the sampling frequency of data acquisition [16][17]. Unless stated differently, the initial conditions for the position (x, y) and velocity (u, v) are chosen on the base path and with velocity V_p in the direction of the curve.

5.2 Calculations

The simulations are performed in python. A simplified version of the python code can be found in Appendix C.

Prior to simulations the following functions have to be defined:

- The function of the base path $\gamma(s)$;
- The tangent vector $\mathbf{T}(s)$ (Equation (3.24));
- The normal vector $\mathbf{N}(s)$ (Equation (3.25));
- The coordinate transformation $\phi(s,h)$ (Equation (3.29));
- The derivatives of $\phi(s,h)$ ($\frac{\partial\phi}{\partial s}$, $\frac{\partial\phi}{\partial h}$, $\frac{\partial^2\phi}{\partial s^2}$ and $\frac{\partial^2\phi}{\partial s\partial h}$);
- The Jacobian of ϕ (J_ϕ) and its inverse $J_{\phi^{-1}}$;
- The derivatives of $J_{\phi^{-1}}$ ($\frac{\partial}{\partial s}J_{\phi^{-1}}$ and $\frac{\partial}{\partial h}J_{\phi^{-1}}$).

These functions are needed to do computations during the simulations. The part in Equation (4.32) which is the most computational expensive are the Christoffel symbols. Every time step, the computation of the Christoffel symbols takes place according to the following steps:

1. Suppose the positional coordinates of chart ϕ_γ (s,h) are known. The Christoffel symbols in chart ϕ_γ, $\overline{\Gamma}_{ij}^k$ are computed with Equation (4.18).
2. The Christoffel symbols in the Cartesian chart, Γ_{ij}^k are computed with Equation (3.12).

The numerical values of the modeling forces in the equation of motion are computed with Equations (4.21), (4.24) and (4.28).

For all the computations, the positional coordinates in chart ϕ_γ, (s,h), must be known. The coordinate transformation is well defined ($\phi : (s,h) \to (x,y)$), however it is not trivial that an expression for the inverse exists. For an approximate but accurate pull back of coordinates x and y, the Newton-Raphson method is used. This method is explained in Section 3.2.3. The coordinates $\mathbf{s}_i = (s_i, h_i)$ at time step $i = 2, 3, ...$ are determined with the following steps:

1. $(s_i, h_i) = (s_{i-1}, h_{i-1})$, $\quad |\hat{\mathbf{s}}_i - \mathbf{s}_i| \approx 3 \cdot 10^{-2}$ m;
2. $(s_i, h_i) = \mathrm{NR}(s_i, h_i)$, $\quad |\hat{\mathbf{s}}_i - \mathbf{s}_i| \approx 9 \cdot 10^{-4}$ m;
3. $(s_i, h_i) = \mathrm{NR}(s_i, h_i)$, $\quad |\hat{\mathbf{s}}_i - \mathbf{s}_i| \approx 8 \cdot 10^{-7}$ m,

where NR($\cdot$) is an iteration of the Newton-Raphson method (Equation (3.30)) and (s_{i-1}, h_{i-1}) are the coordinates at time step $i-1$. The first distance between the exact coordinate $\hat{\mathbf{s}}_i$ and the approximation $\mathbf{s}_i$ is based on the discretization step size of $\frac{1}{30}$ s and the typical walking velocity of around 1 ms^{-1}. The second and third distances are based on the quadratic convergence of the Newton-Raphson method (Equation (3.32)).

For first time step ($i = 1$), the process 5.2 is not possible. For the approximation of coordinate $\hat{\mathbf{s}}_1$, a kd-Tree is used. The nodes of a fine (s, h)-coordinate frame are converted back to (x, y)-coordinates. A simplified visualization of the nodes around a parabolic-shaped base-path can be seen in Figure 5.1. Given a point in Cartesian coordinates, the kd-Tree is able to efficiently find the approximate nearest neighbouring node [18]. The approximate nearest node serves as initial guess for $\hat{\mathbf{s}}_1$. The fineness of the (s, h)-coordinate frame is chosen such that the average closest node is less then 10^{-2} m away.

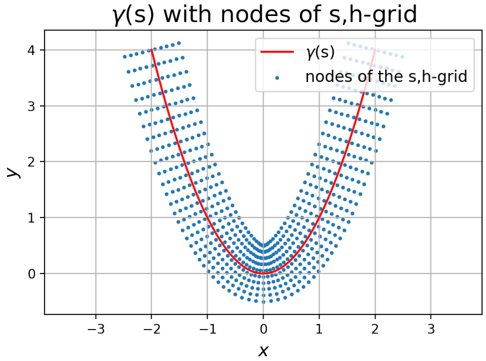

Figure 5.1: A parabolic-shaped base-path with the nodes of a (s, h)-coordinate frame. For visualization purposes, the coordinate frame is not fine. The collection of nodes is used during the kd-Tree nearest node approximation to approximate the initial coordinates (s, h).

6. Validation

The model proposed in Chapter 4 will be validated here. The goal of the model is that it is statistically indistinguishable from reality. This will be investigated by a quantitative comparison of pedestrian dynamics fluctuations with two experiments. In the first experiment, the velocity and position of single pedestrians walking over an elliptical trajectory were measured. The comparison with this experiment will be elaborated in Section 6.1. In the second experiment, pedestrians were tracked during the Glow event in Eindhoven [19]. This experiment will be elaborated in Section 6.2.

6.1 Ellipse experiment

The first experiment was performed at TU/e location “de Markthal” where the velocities and position of pedestrians were measured using Kinect (™Microsoft) depth-cameras [16]. Pedestrians were assigned to follow large elliptical paths, crossing a virtual line on the top and bottom of their path under diluted conditions. A sketch of the top view of this experiment is shown in Figure 6.1. The test originally aimed at quantifying the capability of the tracking sensor to measure pedestrians crossing a line. The fact that pedestrians walk over curved paths makes the data suitable for the quantitative comparison with the proposed model.

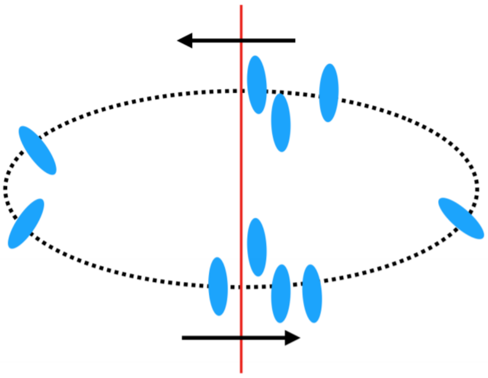

Figure 6.1: A sketch of the top view of the ellipse experiment. Pedestrians (blue) walking in elliptical trajectories while crossing a vertical line (red) at the bottom and top of their path [16].

6.1.1 Refinement of the data set

In Figure 6.2a, the trajectories of the experiment can be seen. Visible are a lot of measurements outside the range of the elliptical trajectory. In order to extract the relevant data from this experiment, the data set should be refined.

The blue rectangle in Figure 6.2b is considered to be the range in which the pedestrians that participated in the experiment were walking. Measured trajectories outside the blue rectangle are removed. Also the short trajectories (i.e. trajectories with less than 250 measurement points) are removed. The remaining trajectories are displayed inside the blue rectangle.

Measured during the experiment are, among other things, the vertical and horizontal velocity components and the vertical and horizontal position of the pedestrians. All unreliable measurement points are also removed from the data set. This are all measurement points where the velocity is faster than 10 ms^{-1} (necessarily measurement errors).

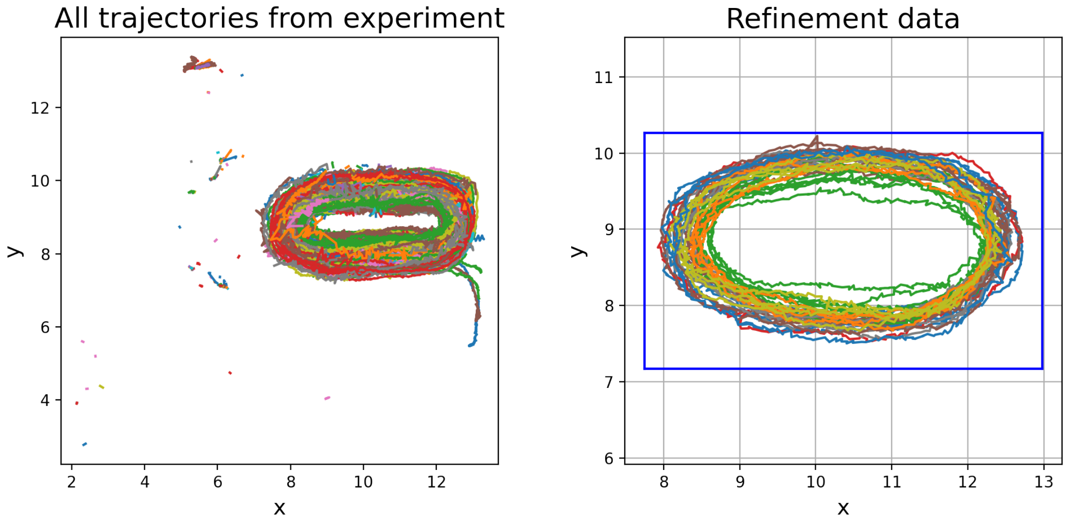

(a) **(b)**

Figure 6.2: All measured trajectories during the ellipse experiment (a) and the refined data set (b).

For simplicity reasons, the whole data set is translated such that the average (x, y)-coordinate of the measurements coincides with the origin.

6.1.2 Average path

The model needs a base-path γ for the simulations. This curve will correspond with the average path of the experiment. In order to find an average path, for each data point the angle between the connection with the origin and the horizontal axis is computed according to:

$$\theta = \arctan\left(\frac{y}{x}\right) \tag{6.1}$$

where x and y are the horizontal and vertical coordinates of the data point respectively.

Because the elliptical-like trajectories of the experiment are periodic, the average path will be estimated with the first six terms of a Fourier series:

$$f(\theta) = a_0 + \sum_{n=1}^{6} [a_n \cos(n\theta) + b_n \sin(n\theta)]. \tag{6.2}$$

This function is fitted for the x-coordinates of the data points as well as the y-coordinates as function of θ. The coefficients of the fitting function f are rounded off and negligible coefficients are neglected. The resulting average paths are:

$$\gamma(\theta) = \begin{cases} x(\theta) = & 0.01\sin(2\theta) + 0.01\sin(4\theta) + 1.68\cos(\theta) + 0.01\cos(2\theta) \\ & +0.29\cos(3\theta) + 0.07\cos(5\theta) + 0.02 \\ y(\theta) = & 1.2\sin(\theta) + 0.02\sin(2\theta) + 0.19\sin(3\theta) + 0.04\sin(5\theta) + 0.01\cos(3\theta) \end{cases} \tag{6.3}$$

where $\theta \in (-\pi, \pi]$. The fit functions $x(\theta)$ and $y(\theta)$ are shown in Figure 6.3. Also curve γ is shown together with the data points of the experiment. The curve $\gamma(s)$ will be used for the model proposed in Section 4, where $s \equiv \theta$.

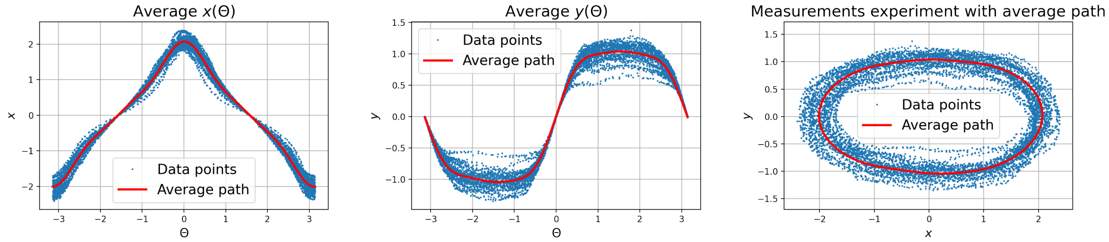

(a) **(b)** **(c)**

Figure 6.3: Graphs of the data points with the average paths of $x(\theta)$ (a), $y(\theta)$ (b) and the plot in Cartesian coordinates with the average path $\gamma = (x(\theta), y(\theta))$ (c).

6.1.3 Calibration of the model

For a comparison between the model and the data of the experiment, a calibration of the model is needed. The parameters of the model, $\{\alpha, \beta, \mu, V_p, \sigma\}$, should be estimated in order to produce comparable trajectories.

The parameter V_p is the preferred velocity in the longitudinal direction. The value of V_p is considered to be the average longitudinal velocity of the experimental data which results in

$$V_p = 1.14\text{ms}^{-1} \tag{6.4}$$

The key of the quantitative comparison will be the relevant probability functions of the position and velocity of the pedestrians. The relevant observables are the transversal and longitudinal velocity ($V_\perp$ and $V_\parallel$ resp.) and the deviation from the average path (h). Equations for the transversal and longitudinal dynamics can be obtained by:

$$\dot{V}_\perp = \langle \dot{\mathbf{u}}, \mathbf{N} \rangle = -2\beta h - 2\mu V_\perp + \sigma \dot{W} \tag{6.5}$$

and

$$\dot{V}_\parallel = \langle \dot{\mathbf{u}}, \mathbf{T} \rangle = -8\alpha V_p^2 (V_\parallel - V_p) + \sigma \dot{W}. \tag{6.6}$$

The velocity fluctuations of pedestrians that are investigated have a typical frequency around 1 Hz. Because the terms $\langle \Gamma^k_{ij} u^i u^j, \mathbf{T} \rangle$ and $\langle \Gamma^k_{ij} u^i u^j, \mathbf{N} \rangle$ should compensate the fact that the path is curved, they have a periodicity equal to the periodicity of the curve. This can also be seen in Figure 6.4. In this figure, the numerical value of the terms $\langle \Gamma^k_{ij} u^i u^j, \mathbf{T} \rangle$ and $\langle \Gamma^k_{ij} u^i u^j, \mathbf{N} \rangle$ are shown during a simulation along the base path. The period of the Christoffel symbol terms is around 10 seconds which corresponds to 0.1 Hz. Since this is much smaller than the typical frequency of velocity fluctuations, the contribution to the distribution of the dynamics is neglected. Therefore, terms $\langle \Gamma^k_{ij} u^i u^j, \mathbf{T} \rangle$ and $\langle \Gamma^k_{ij} u^i u^j, \mathbf{N} \rangle$ are left out Equations (6.6) and (6.5).

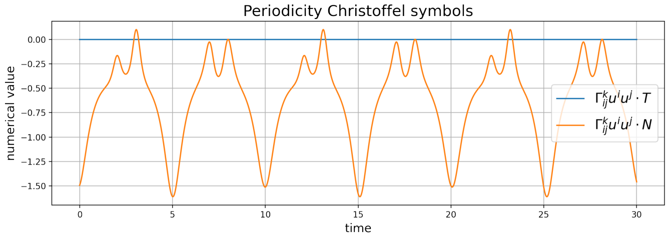

Figure 6.4: The numerical value of the terms the Christoffel terms $\langle \Gamma^k_{ij} u^i u^j, \mathbf{T} \rangle$ and $\langle \Gamma^k_{ij} u^i u^j, \mathbf{N} \rangle$ is plotted against the time during a force-free simulation along the base path Equation (6.3)). Visible is the periodicity of these terms with a period around 10 seconds.

In the stationary regime, the probability distribution of the transversal velocity and transversal deviation from the base-path, $P(h, V_\perp)$, follow the well-known Fokker-Planck equation (e.g. [4] or

[20]) with solutions

$$\begin{aligned} P(h, V_\perp) = P(h)P(V_\perp) &= \mathcal{N} \exp\left[-\frac{\Phi_{V_\perp}(V_\perp)}{\sigma^2/2} - \frac{2\gamma \Phi_h(h)}{\sigma^2/2}\right] \\ &= \mathcal{N} \exp\left[-\frac{2\mu}{\sigma^2}V_\perp^2 - \frac{4\beta\mu}{\sigma^2}h^2\right] \end{aligned}, \tag{6.7}$$

where $\Phi_{V_\perp}$ and Φ_h are the confinement potentials (Equations (4.23) and (4.20)) and $\mathcal{N}$ a normalisation constant. A potential can be constructed according to $\Phi(\cdot) = -\ln(P(\cdot))$. The empiric and analytical potential of the transversal dynamics should be similar in order to make a comparison. Therefore, the ratios $\frac{2\mu}{\sigma^2}$ and $\frac{4\beta\mu}{\sigma^2}$ are compared with the observables according to

$$-\ln(P_{exp}(V_\perp)) \approx \frac{2\mu}{\sigma^2}V_\perp^2 + K_1 \tag{6.8}$$

and

$$-\ln(P_{exp}(h)) \approx \frac{2\mu}{\sigma^2}h^2 + K_2. \tag{6.9}$$

The constants K_1 and K_2 are normalisation constants and $P_{exp}(a)$ is the empiric probability function of observable a obtained from the experimental data. In Figure 6.5, the latter relations are compared. The ratios $\frac{2\mu}{\sigma^2}$ and $\frac{4\beta\mu}{\sigma^2}$ are fitted such that the empiric potential and analytical potential of the model are similar. The resulting estimated ratios are

$$\frac{2\mu}{\sigma^2} \approx 4.83 \tag{6.10}$$

and

$$\frac{4\beta\mu}{\sigma^2} \approx 20.94. \tag{6.11}$$

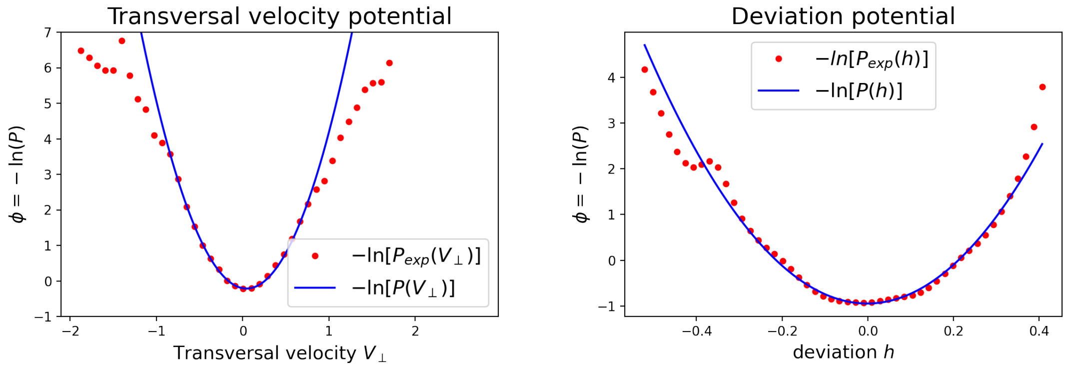

(a) (b)

Figure 6.5: The transversal velocity potential is achieved from the empiric probability function with the analytical velocity potential fitted (Equation (6.8)) (a). The deviation potential is also achieved empirically. The fitted analytical deviation potential is also plotted (Equation (6.9)) (b).

The same can be done for the longitudinal dynamics (Equation (6.5)). In the stationary regime, the probability of the longitudinal velocity is distributed according to [4]

$$P(V_\parallel) = \mathcal{N} \exp\left[-\frac{\Phi_{V_\parallel}(V_\parallel)}{\sigma^2/2}\right] = \mathcal{N} \exp\left[\frac{8\alpha V_p^2}{\sigma^2}(V_\parallel - V_p)^2\right] \tag{6.12}$$

where $\mathcal{N}$ is a normalisation constant and $\Phi_{V_\parallel}$ the longitudinal velocity potential of Equation (4.26). The ratio $\frac{8\alpha}{\sigma^2}$ is compared to the empirical distribution function of the longitudinal velocity by

$$-\ln\left(P_{exp}(V_\parallel)\right) \approx \frac{8\alpha}{\sigma^2}V_p^2\left(V_\parallel - V_p\right)^2 + K_3. \tag{6.13}$$

Constant K_3 is again for normalisation. Similarly as for the transversal dynamics, the ratio $\frac{8\alpha}{\sigma^2}$ is fitted. The empiric potential with the fitted analytical potential is shown in Figure 6.6a. The resulting value of the ratio is

$$\frac{8\alpha}{\sigma^2} \approx 2.52. \tag{6.14}$$

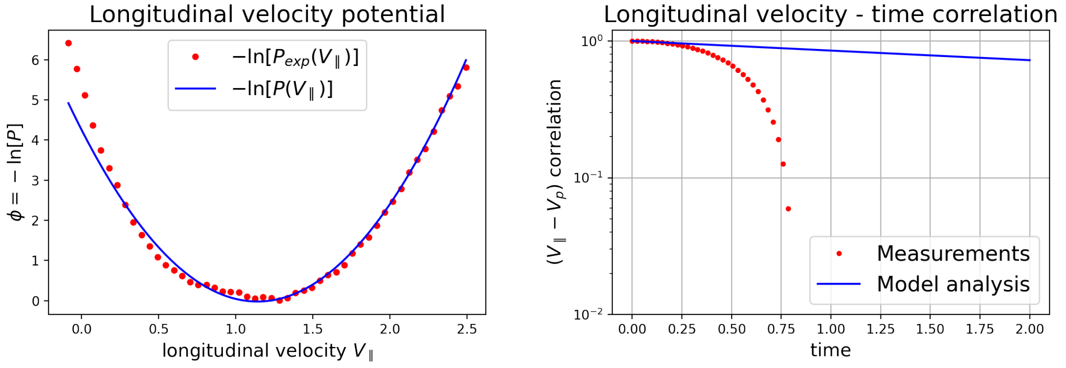

(a) **(b)**

Figure 6.6: In (a), the longitudinal velocity potential is plotted for the experimental values and the analytical values of the model. The analytical longitudinal velocity potential is fitted to resemble the empirical potential. In (b), the empirical time correlation is shown for observable $(V_\parallel - V_p)$ and the the analytical time correlation ($\sim \exp\left(-8\alpha V_p^2 t\right)$) is fitted.

To complete the parameter estimation, a time correlation function is used. First, Equation (6.5) is written as

$$\frac{d}{dt}\left(V_\parallel - V_p\right) = -8\alpha V_p^2 \left(V_\parallel - V_p\right) + \sigma \dot{W}. \tag{6.15}$$

According to this equation, the time correlation function of $\left(V_\parallel - V_p\right)$ should decay as $\exp\left(-8\alpha V_p^2 t\right)$. Since α is the only unknown parameter in this equation, it can be estimated by a comparison with the time correlation of the experimental data.

The time correlation function $C_\Xi(t)$ for a generic observable Ξ is [4]

$$C_\Xi(t) = \frac{\mathbf{E}_\gamma\left[\tilde{\Xi}^\gamma_{t_0} \cdot \tilde{\Xi}^\gamma_t\right] - \mathbf{E}_\gamma\left[\tilde{\Xi}^\gamma_{t_0}\right] \cdot \mathbf{E}_\gamma\left[\tilde{\Xi}^\gamma_t\right]}{\sqrt{N\left(t_0\right) \cdot N(t)}} \tag{6.16}$$

where $\mathbf{E}_\gamma$ denotes the average over the trajectory ensemble and function N(t) is given by

$$N(t) = \mathbf{E}_\gamma\left[\left(\tilde{\Xi}^\gamma_t - \mathbf{E}_\gamma\left[\tilde{\Xi}^\gamma_t\right]\right)^2\right]. \tag{6.17}$$

Denoted is Ξ^γ_t for the value of observable Ξ that trajectory γ has at time t. Also, $\tilde{\Xi}^\gamma_t = \Xi^\gamma_t - \mathbf{E}_t\left[\Xi^\gamma_t\right]$ is denoted for the fluctuating component of Ξ.

The empirical time correlation function of observable $\left(V_\parallel - V_p\right)$ is shown in Figure 6.6b. To obtain the empirical time correlation function, the high frequency fluctuations were filtered out the measured longitudinal velocity. The dynamics of pedestrians have fluctuations of 0-2.5 Hz [16]. Fluctuations with higher frequencies are the result of measurement noise. Therefore, all frequencies larger then 2.5 Hz are filtered out using the Fourier transform.

The vertical axis is logarithmic scaled so the analytical time correlation is a straight line. Parameter α is fitted in such a way that the analytical time correlation resembles the empirical time correlation in the beginning. The resulting value of α is

$$\alpha \approx 0.046 \text{ m}^{-2}\text{s} \tag{6.18}$$

With Equations (6.10), (6.11), (6.14) and (6.18) the parameters of the model can be estimated. The resulting values of the parameters can be found in Table 6.1.

Table 6.1: The values of the parameters of the model. Longitudinal propulsion scale parameter α, transversal confinement scale parameters β and μ, preferred longitudinal velocity V_p and noise scale parameter σ.

Parameter	Value	Unit
α	0.046	$\mathrm{m}^{-2}\mathrm{s}$
β	2.17	$\mathrm{m}^{2}\mathrm{s}$
μ	0.35	s^{-1}
V_p	1.14	ms^{-1}
σ	0.38	$\mathrm{ms}^{-3/2}$

6.1.4 Comparison

The model proposed in Section 4 with curve $\gamma(s)$ from Equation (6.3) and the estimated parameters of Table 6.1 is used for long simulations. In figure 6.7a, an example of a simulation by the model is shown as well as a measured trajectory.

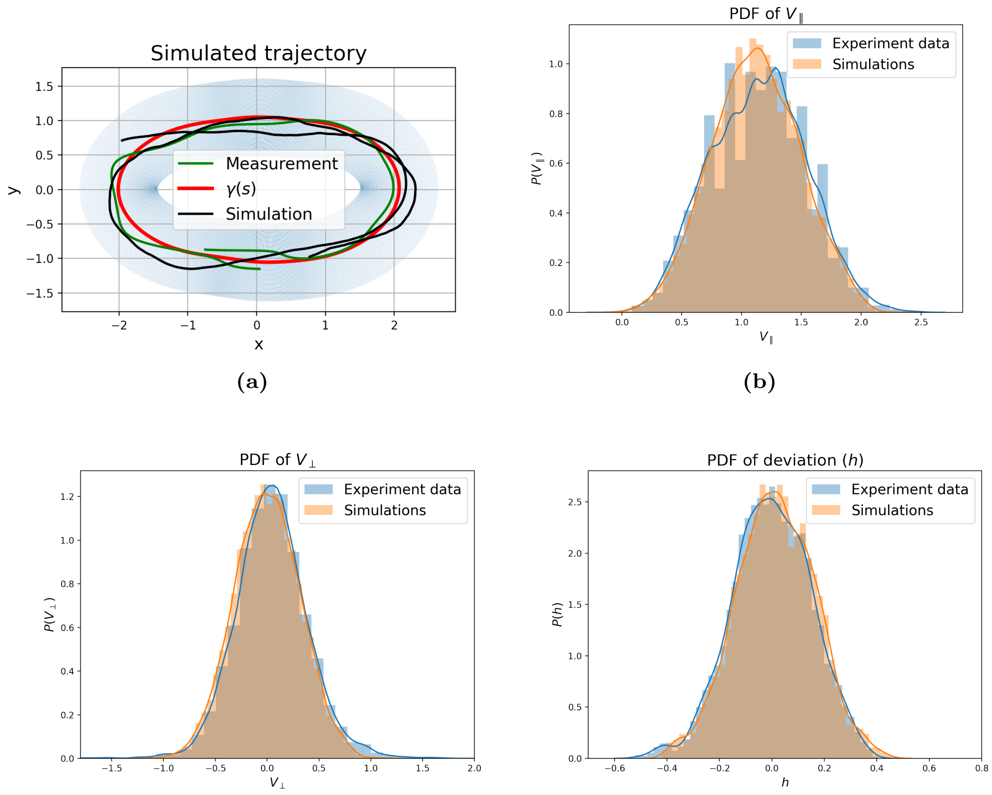

(a) (b) (c) (d)

Figure 6.7: In (a), an example of a simulated trajectory along the average path γ is displayed. (b)-(d) show the probability density functions of the longitudinal velocity $V_\parallel$, the transversal velocity $V_\perp$ and the deviation h. The blue histograms are empirically determined from the experiment data. The orange histograms are obtained from the simulations. The curves through the histograms are the kernel density estimations.

The probability density functions of the relevant observables are obtained from the simulations by the model. The relevant observables are the longitudinal velocity $V_\parallel$, the transversal velocity

$V_\perp$ and the deviation from the curve h. The probability density functions are shown in Figure 6.7b, 6.7c and 6.7d. It can be seen that the probability distributions of the simulations and the experiment data are very similar. These graphs substantiate that the model is statistically indistinguishable from the experiment.

6.2 Glow experiment

Another experiment that has been performed is a experiment during the Glow festival in November 2017 (Eindhoven, the Netherlands) [19]. The velocity and position of pedestrians was tracked while pedestrians were walking in a corridor. The experiment took place for a couple of days so a lot of data is available. However, only a small portion (1 minute) will be used in this thesis for a glance of the model performance. In Figure 6.8a, the measured trajectories are shown. Most of the trajectories start at the bottom of the figure and the pedestrians walk upwards. It can be seen that there is a large obstacle in the middle of the corridor because all trajectories avoid the middle. Interesting are the trajectories that start below the obstacle. These paths are curved as the pedestrians must curve their trajectory to avoid the obstacle. The bending of the paths makes this experiment suitable for validation of the proposed model. Neglected will be the fact that the pedestrian motions are not diluted.

Refinement of the data set

For the refinement of the data, all measured trajectories outside the red vertical lines in Figure 6.8a is considered to be noise. Furthermore all short trajectories (i.e. trajectories that cover less than 10m vertical distance) and trajectories that are downwards are removed from the data set. Finally the data points that contain measurement errors are removed.

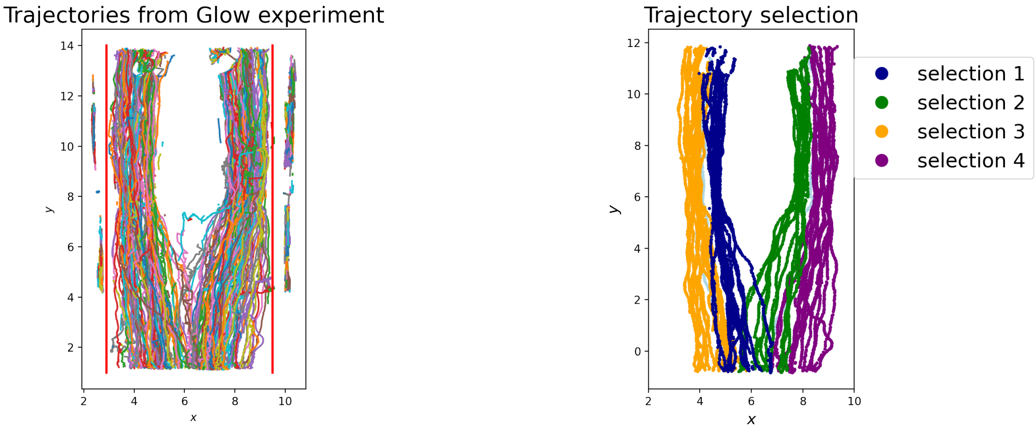

(a) **(b)**

Figure 6.8: In (a): The whole data set. Visible is noise outside the red vertical lines. In (b): all trajectories after the refinement of the data set divided into four selections. Selection 1 is displayed in dark blue and passes the obstacle on the left hand side. Selection 2 is displayed in green and passes the obstacle on the right hand side. Selections 3 and 4 in orange and purple respectively, pass the obstacle at the boundaries of the corridor.

Average path

For the model to work, a curve γ is needed which serves as base-path. Since this experiment takes place in a broad corridor, there are several different paths next to each other. In order to find an average path, selections of trajectories needs to be made in which the trajectories look similar. Four selections have been made:

- Selection 1: trajectories that pass the obstacle on the left hand side and close to the obstacle (at a distance of 0.5m at height $y = 6$m);

- Selection 2: trajectories that pass the obstacle on the right hand side and close to the obstacle (0.9m at height $y = 6$m);

- Selection 3: trajectories that pass the obstacle on the left hand side and close to the boundary of the corridor (0.9m at height $y = 6$m);

- Selection 4: trajectories that pass the obstacle on the right hand side and close to the boundary of the corridor (0.9m at height $y = 6$m).

In Figure 6.8b, the four selections are shown in dark blue, green, orange and purple.

The average path will be estimated with the first terms of a Fourier series:

$$g(y) = a_0 + \sum_{n=1}^{4} \left[a_n \cos\left(n\frac{2\pi}{18}y\right) + b_n \sin\left(n\frac{2\pi}{18}y\right)\right]. \tag{6.19}$$

The function g is fitted for the x-coordinates of the data points as function of the y-coordinates. The period of function g is equal to 18 which is larger than the length of the corridor. After rounding off the coefficients and neglecting the negligible coefficients, the resulting average paths are:

$$\gamma_1(s) = \begin{cases} x(s) = 0.48\cos\left(\frac{\pi}{9}s\right) + 0.14\cos\left(\frac{2\pi}{9}s\right) + 4.97 \\ y(s) = s \end{cases}, \tag{6.20}$$

$$\gamma_2(s) = \begin{cases} x(s) = & -0.69\sin\left(\frac{\pi}{9}s\right) - 0.25\sin\left(\frac{2\pi}{9}s\right) + 0.32\sin\left(\frac{3\pi}{9}s\right) + 0.1\sin\left(\frac{4\pi}{9}s\right) \\ & -0.55\cos\left(\frac{\pi}{9}s\right) - 0.62\cos\left(\frac{2\pi}{9}s\right) - 0.19\cos\left(\frac{3\pi}{9}s\right) + 7.75 \\ y(s) = s & \end{cases}, \tag{6.21}$$

$$\gamma_3(s) = \begin{cases} x(s) = 0.43\cos\left(\frac{\pi}{9}s\right) + 4.1 \\ y(s) = s \end{cases} \tag{6.22}$$

and

$$\gamma_4(s) = \begin{cases} x(s) = 0.32\sin\left(\frac{\pi}{9}s\right) + 0.18\sin\left(\frac{2\pi}{9}s\right) - 0.56\cos\left(\frac{\pi}{9}s\right) + 0.12\cos\left(\frac{3\pi}{9}s\right) + 8.3 \\ y(s) = s \end{cases} \tag{6.23}$$

where $\gamma_1(s)$, $\gamma_2(s)$, $\gamma_3(s)$ and $\gamma_4(s)$ are the average paths for selection 1, 2, 3 and 4 respectively. The advantage of the fact that all average paths are periodic is that simulations encounter the same corridor over and over again. The average paths are displayed in Figure 6.9.

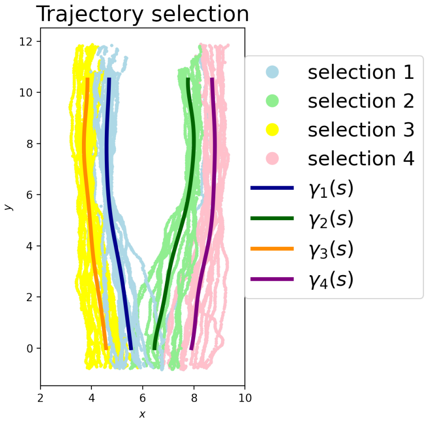

Figure 6.9: The measured trajectories of the glow experiment visualized in light colors. The average path of each selection is displayed in darker colors.

Calibration of the model

Again, the parameters of the model, $\{\alpha, \beta, \mu, V_p, \sigma\}$, should be estimated for a good validation. This will be done four times (once for each selection) and similarly as in Section 6.1.3. The data at $y < 2$ and $y > 10.5$ will not be considered for the parameter estimation as well as the comparison because the trajectories are clearly distributed differently in this area.

The empirical potentials and time correlation with the analytical fits that are used for the parameter estimation can be found Appendix A. With the fitted ratios for the longitudinal and transversal dynamics, the values of the parameters can be estimated. The estimated values of the parameters can be found in Table 6.2.

Table 6.2: The values of the parameters of the model used for the glow experiment. A distinction is made between trajectory selection 1 an selection 2. The parameters are the Longitudinal propulsion scale parameter α, transversal confinement scale parameters β and μ, preferred longitudinal velocity V_p and noise scale parameter σ.

Parameter	selection 1	selection 2	selection 3	selection 4	Unit
α	0.029	0.040	0.033	0.046	$\mathrm{m}^{-2}\mathrm{s}$
β	1.40	0.67	0.55	0.47	$\mathrm{m}^{2}\mathrm{s}$
μ	0.26	0.23	0.29	0.31	s^{-1}
V_p	1.25	1.13	1.25	1.09	ms^{-1}
σ	0.29	0.30	0.32	0.31	$\mathrm{ms}^{-3/2}$

Comparison

The estimated parameters of Table 6.2 and the curves of Equations (6.20) and (6.21) are used in the proposed model of Section 4. Long simulations have been performed. Only the data of the simulations is used that cover the relevant part of the corridor. Several of the simulated trajectories can be seen in Figure 6.10.

Figure 6.11 shows the obtained probability density functions of the relevant observables of selection 1 ($V_{\|}$, $V_{\perp}$ and h) in comparison with the corresponding empiric density functions. The probability density functions of the experiment data and the simulations are alike, but not the extent of the ellipse experiment. Plausible is that the the widths of the selection are too wide. As a consequence, pedestrians do not fluctuate along the base-path but along a parallel path.

Furthermore, the fact that interactions with other pedestrians, obstacles and walls is neglected, can cause deviations between the simulations and the measurements. Because of the diluted conditions in the ellipse experiment, interactions were not present there.

Lastly, in the size of the data set is room for improvement. If the whole duration of the experiment is used, the resemblance could be different.

The probability density functions of the other selections are shown in Appendix B. In the other selections, it can also be seen that the empiric and simulated probability density functions show worse agreement.

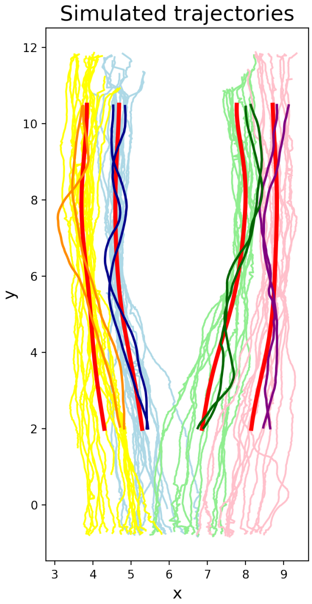

Figure 6.10: Simulated trajectories for the glow experiment in different selections. Simulated trajectories of selection 1 are shown in dark blue and selections 2, 3 and 4 in green, orange and purple respectively. In the lighter colors, the measured trajectories are shown.

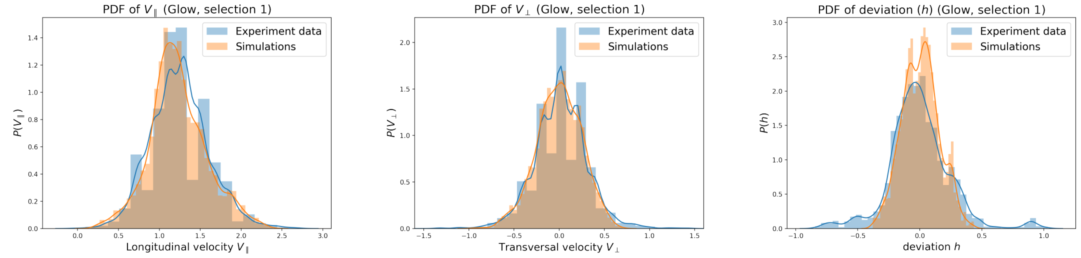

(a) **(b)** **(c)**

Figure 6.11: The probability density functions of selection 1 of the observables: longitudinal velocity $V_\parallel$ (a), transversal velocity $V_\perp$ and deviation from the average path h.

7. Discussion and conclusion

This thesis proposes a model that quantitatively predicts fluctuations of pedestrian dynamics in curved and diluted pedestrian flows. The proposed model is force-based which already has been applied to straight paths [4]. With differential geometry, straight lines were redefined to be, possibly curve, geodesics. This made it possible to create a model for curved base-paths. Confinement forces, longitudinal propulsion and Gaussian noise are the added modeling forces for realistic pedestrian behaviour.

The proposed model was validated in Chapter 6 using the data of two experiments. The quantitative comparison with the ellipse experiment showed a good agreement between the empiric and simulated probability density functions of relevant fluctuations. The investigated fluctuations that pedestrian motions feature are fluctuations in longitudinal velocity, transversal velocity and deviation relative to the base-path.

The comparison with the experiment during Glow 2017 on the other hand, showed worse agreement. Probable causes are the choice of trajectory selection, the quantity of data that was investigated or the interactions that pedestrian might have with other pedestrians, obstacles or walls during the experiment. Still, the results are promising and the validation of the proposed model with this experiment is worth using for further research.

Limitations

The model that is proposed in this thesis shows promising results regarding the quantitative comparison with real life data. The produces distributions of relevant fluctuations agrees with the distribution of real life pedestrian fluctuations. However the model has some limitations that are noteworthy to discuss:

- One limitation is that the model is limited to the diluted scenario. Other pedestrians could affect the fluctuations of pedestrian dynamics such that the model would not be able to adapt. In reality, pedestrians interact with obstacles or other pedestrians very often;
- The model assumes that the potentials of the modeling forces are uniform over the base-path. However, in many scenarios pedestrians should be confined differently at certain sections of the base-path. For example, when a narrow corridor is approached, the confinement potential is expected to become steeper;
- The model needs a base-path for simulations. In reality, most pedestrians do not always stick to a certain base path. For instance, when the corridor of the glow experiment is crossed from left to right, the trajectory does not belong in one of the selections (Figure 6.8b).

Further research

The limitations of the model generate ideas for further research. The limitation of the model to diluted conditions arises the question how other pedestrians or obstacles curve the intended path of a pedestrian. In other words, how do pedestrians or obstacles affect the geometry? An answer to this question is needed to bring the proposed model to dense pedestrian flows.

Secondly, From the data acquisition of the Glow event, it could be seen that the properties of the trajectories change over the course of the corridor. For example, the trajectories of a selection converge when the obstacle is approached. The parameters of the model could be made time or position dependent for a better correspondence with the real life data.

To conclude, the proposed model, limited to diluted conditions, seems able to quantitatively reproduce the fluctuating behaviour of single pedestrians in curved motions. However, further research is needed to bring the model to more complex pedestrian situations.

8. Acknowledgement

Hereby, I would like to express my gratitude towards my supervisors prof. F. Toschi, dr. A. Corbetta and prof. W. Schilders. Their guidance and involvement helped me a lot with the progress towards this bachelor thesis.

Bibliography

[1] V. Gaia. Cities: How crowded life is changing us, 2013. URL `https://www.bbc.com/future/article/20130516-how-city-life-is-changing-us`. 1

[2] S. Dowling. 2050: Building better cities for an overcrowded world, 2013. URL `https://www.bbc.com/future/article/20130507-challenges-for-the-cities-of-2050`. 1

[3] P. Kachroo. Pedestrian Dynamics: Mathematical Theory and Evacuation Control., 2010. 1

[4] A. Corbetta, C. Lee, R. Benzi, A. Muntean, and F. Toschi. Fluctuations around mean walking behaviors in diluted pedestrian flows. *Phys. Rev. E*, 95:032316, Mar 2017. doi: 10.1103/PhysRevE.95.032316. URL `https://link.aps.org/doi/10.1103/PhysRevE.95.032316`. 1, 2, 13, 18, 27, 28, 29, 35

[5] D. Helbing and P. Molnár. Social force model for pedestrian dynamics. *Phys. Rev. E*, 51: 4282–4286, May 1995. doi: 10.1103/PhysRevE.51.4282. URL `https://link.aps.org/doi/10.1103/PhysRevE.51.4282`. 2

[6] L. Florack. Course notes tensor calculus and differential geometry 2wah0, 2020. URL `https://www.win.tue.nl/~lflorack/Extensions/2WAH0CourseNotes.pdf`. 5

[7] L.P. Lebedev, M.J. Cloud, and V.A. Eremeyev. *Tensor Analysis With Applications In Mechanics.*, volume [New ed.]. World Scientific, 2010. ISBN 9789814313124. URL `http://search.ebscohost.com/login.aspx?direct=true&db=nlebk&AN=340814&site=ehost-live`. 6, 10

[8] J. Simmonds. A Brief on Tensor Analysis, 1994. URL `https://doi.org/10.1007/978-1-4419-8522-4`. 6

[9] A. Gray. *Tubes.* Birkhauser, 2nd ed. edition, 2004. ISBN 3764369078 9783764369071. URL `https://doi-org.dianus.libr.tue.nl/10.1007/978-3-0348-7966-8`. 9

[10] A. Ben-Israel. A newton-raphson method for the solution of systems of equations. *Journal of Mathematical analysis and applications*, 15(2):243–252, 1966. 11

[11] S. Akram and Q. Ann. Newton raphson method. *International Journal of Scientific & Engineering Research*, 6(7):1748–1752, 2015. 11

[12] E. Pardoux and A. Rascanu. Stochastic Differential Equations, Backward SDEs, Partial Differential Equations, 2014. URL `https://doi.org/10.1007/978-3-319-05714-9`. 11

[13] X. Mao. Stochastic differential equations and applications, 2008. URL `https://www.sciencedirect.com/science/book/9781904275343http://vh7qx3xe2p.search.serialssolutions.com/?V=1.0{&}L=VH7QX3XE2P{&}S=JCs{&}C=TC0001114770{&}T=marc{&}tab=BOOKS`. 12

[14] Y. A. Alnafisah. First-order numerical schemes for stochastic differential equations using coupling. 2016. 12

[15] A. Rößler. Runge–kutta methods for the strong approximation of solutions of stochastic differential equations. *SIAM Journal on Numerical Analysis*, 48(3):922–952, 2010. 12, 23

[16] prof. F. Toschi J. Willems, dr. A. Corbetta. Quantifying the quality of pedestrian trajectory measurements: Prorail consultancy report, 2019. 23, 25, 29

[17] J. Willems, A. Corbetta, V. Menkovski, and F. Toschi. Pedestrian orientation dynamics from high-fidelity measurements. *Scientific Reports*, 10(1):11653, 2020. ISSN 2045-2322. doi: 10.1038/s41598-020-68287-6. URL `https://doi.org/10.1038/s41598-020-68287-6`. 23

[18] J.L. Bentley. Multidimensional binary search trees used for associative searching. *Communications of the ACM*, 18(9):509–517, 1975. 24

[19] A. Corbetta, W. Kroneman, M. Donners, A. Haans, P. Ross, M. Trouwborst, S. Van de Wijdeven, M. Hultermans, D. Sekulovski, F. van der Heijden, S. Mentink, and F. Toschi. A large-scale real-life crowd steering experiment via arrow-like stimuli. *Collective Dynamics*, 5:61–68, 2020. ISSN 2366-8539. doi: 10.17815/CD.2020.34. URL `https://collective-dynamics.eu/index.php/cod/article/view/A34`. 25, 31

[20] J. L. Garcia-Palacios. Introduction to the theory of stochastic processes and brownian motion problems. 2007. URL `http://arxiv.org/abs/cond-mat/0701242`. 28

A. Appendix: Calibration (Glow)

This Appendix contains the empiric potentials (transversal deviation, transversal velocity and longitudinal velocity) of the Glow experiment (Section 6.2). The analytical potentials of the model are scaled such that it more or less coincides with the empiric potential. Also, the time correlation of the longitudinal velocity is shown with the analytical time correlation fitted. These fits are used for the estimation of the parameters. The parameters are estimated for each selection (Figure 6.8b) separately.

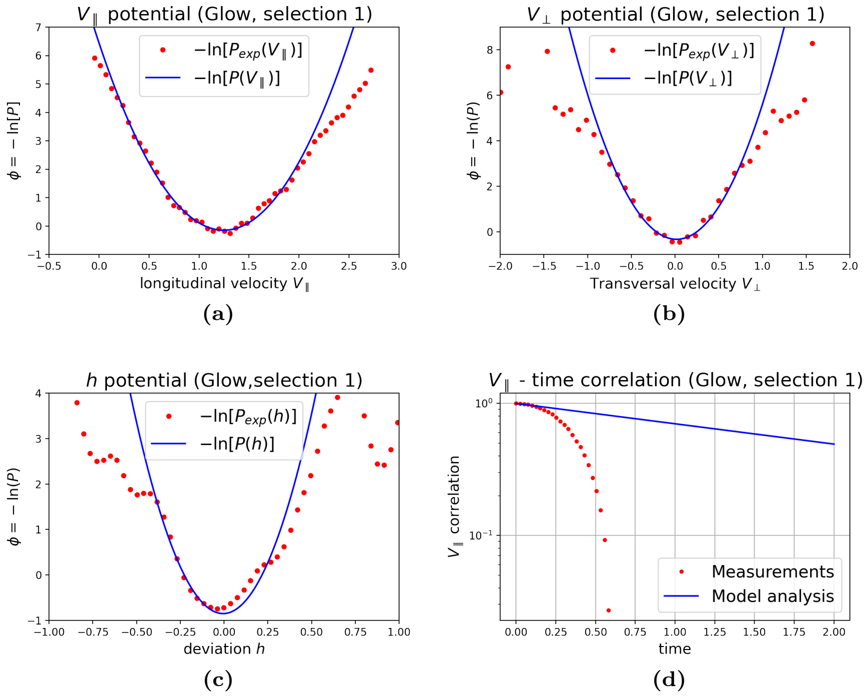

(a) **(b)** **(c)** **(d)**

Figure A.1: The graphs of the empirical longitudinal velocity potential (a), transversal velocity potential (b), deviation potential (c) and $V_\parallel$-time correlation (d) with the corresponding analytical fits used for the parameter estimation of selection 1 of the Glow experiment.

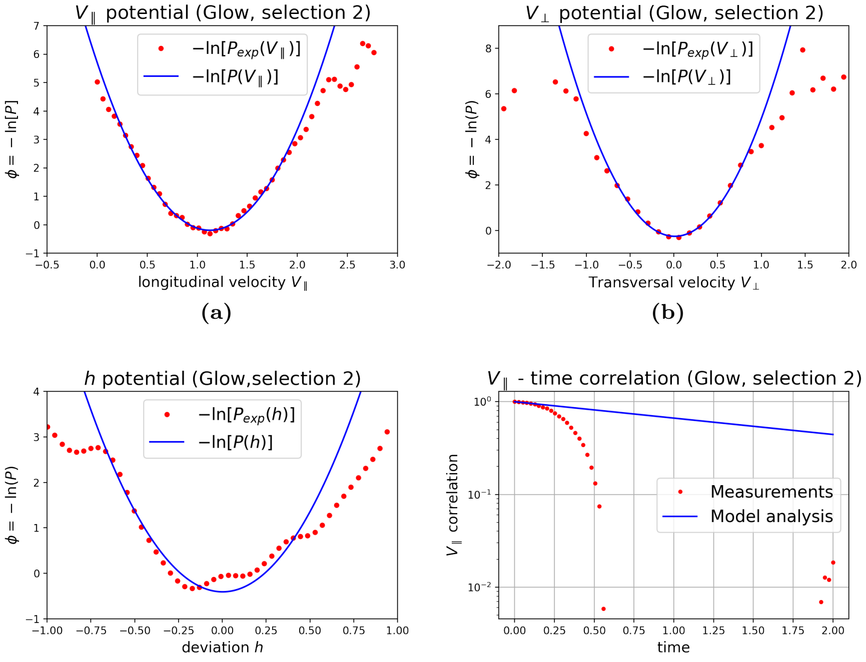

(a) **(b)**

(c) **(d)**

Figure A.2: The graphs of the empirical longitudinal velocity potential (a), transversal velocity potential (b), deviation potential (c) and $V_\parallel$-time correlation (d) with the corresponding analytical fits used for the parameter estimation of selection 2 of the Glow experiment.

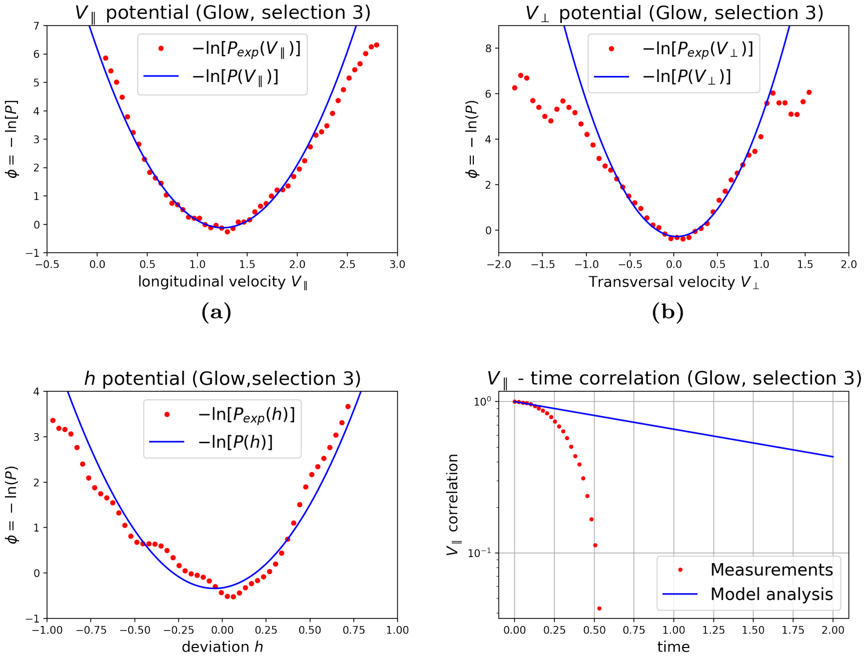

(a) **(b)**

(c) **(d)**

Figure A.3: The graphs of the empirical longitudinal velocity potential (a), transversal velocity potential (b), deviation potential (c) and $V_\parallel$-time correlation (d) with the corresponding analytical fits used for the parameter estimation of selection 3 of the Glow experiment.

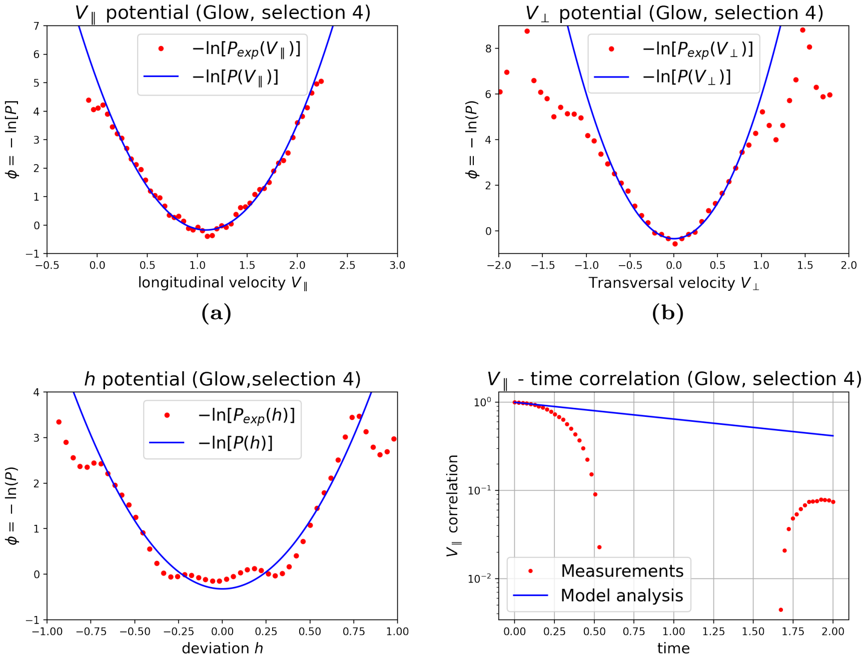

(a) **(b)** **(c)** **(d)**

Figure A.4: The graphs of the empirical longitudinal velocity potential (a), transversal velocity potential (b), deviation potential (c) and $V_\parallel$-time correlation (d) with the corresponding analytical fits used for the parameter estimation of selection 4 of the Glow experiment.

B. Appendix: Comparison (Glow experiment)

This Appendix contains the probability density functions of the longitudinal velocity, transversal velocity and transversal deviation of the Glow experiment (Section 6.2). The probability distribution is shown for the measurements as well as the simulations by the calibrated model. The distribution functions for selection 1 can be found in Figure 6.11. The probability functions of the other selections can be found here.

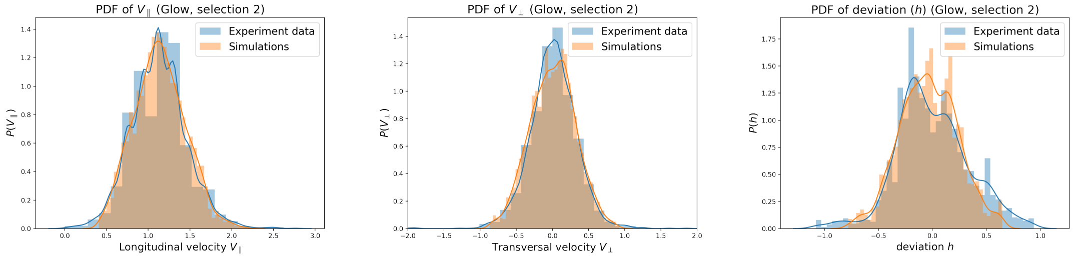

(a) **(b)** **(c)**

Figure B.1: The empiric and simulated probability density functions of selection 2 of the observables: longitudinal velocity $V_\parallel$ (a), transversal velocity $V_\perp$ and deviation from the average path h.

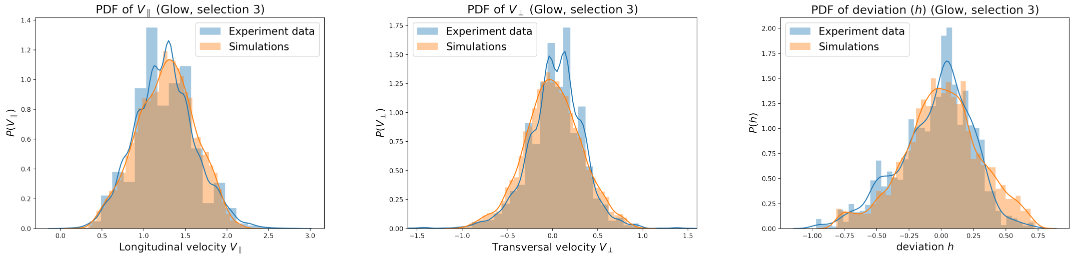

(a) **(b)** **(c)**

Figure B.2: The empiric and simulated probability density functions of selection 3 of the observables: longitudinal velocity $V_\parallel$ (a), transversal velocity $V_\perp$ and deviation from the average path h.

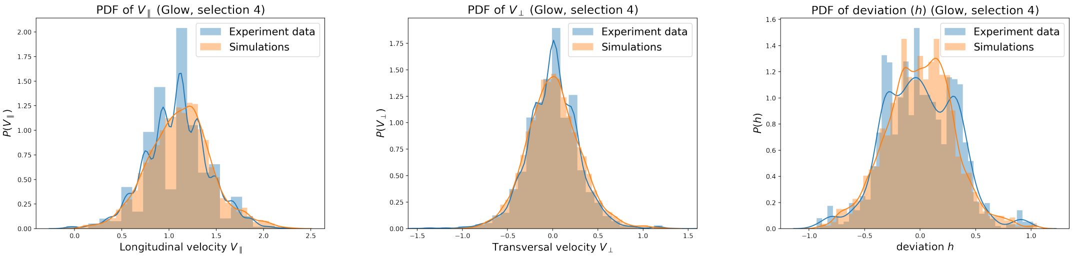

(a) **(b)** **(c)**

Figure B.3: The empiric and simulated probability density functions of selection 4 of the observables: longitudinal velocity $V_\parallel$ (a), transversal velocity $V_\perp$ and deviation from the average path h.

C. Appendix: Pseudo-code simulations

The pseudo-code in Figure C.1 shows the relevant function that are needed during simulations. The first function that is defined (`Christoffel(s,h)`) computes the Jacobian matrix, the inverse Jacobian matrix and relevant derivatives. Then the function computes the Christoffel symbols in the (s, h)-parametrization according to Equation (4.18) and converts them to Cartesian coordinates with Equation (3.12).

The second function (`model(z,t)`) contains all computations needed for the equation of motion (Equation (4.32)). First it converts the (x, y)-coordinates to (s, h)-coordinates with the Newton-Raphson method. A detailed description of this can be found in Chapter 5. Then, the Christoffel symbols are determined with the function `Christoffel(s,h)`. Next, the numerical values of the confinement and propulsion force will be calculated with the Equations (4.21), (4.24) and (4.28). Finally, the function computes the accelerations in x and y. In the last lines, the Einstein summation convention is used by abuse of notation and `C[k,i,j]` is denoted for Γ^k_{ij}.

The first guess of the s and h coordinate is done with the kd-Tree method (denoted as `phi-inv(xi,yi)`). This is elaborately explained in Chapter 5.

The function `Noise(x,t)` contains the noise parameters σ.

Lastly, the equation of motion, which is a system of four SDE's will be solved with the Runge-kutta algorithm SRI2 (Chapter 5).

```
def Christoffel(s,h): # Calculates Christoffel symbols

    # Compute relevant function values
    Compute J(s,h)
    Compute J_inv(s,h)
    Compute J_inv_s(s,h)
    Compute J_inv_h(s,h)

    # Compute Christoffel symbols in (s,h)
    Compute C_sh = Array([[[C_s_ss(s,h),C_s_sh(s,h)],[C_s_hs(s,h),0]],[[0,0],[0,0]]])

    # Push Christoffel symbols forward to (x,y)
    Contract C = J * J_inv * J_inv * C_sh + J * J_inv_i
    return C


def model(z,t):
    x,y,xdot,ydot = z

    # Compute coordinates s and h
    (s,h)=(d['s'],d['h']) # Obtain previous value of (s,h)
    (s,h) = Newton(s,h,x,y) # Newton Raphson method to approximate current (s,h)
    (s,h) = Newton(s,h,x,y)
    d['s'],d['h']=s,h # Store (s,h) for next timestep

    # Compute Christoffel symbols
    C = Christoffel(s,h)

    # Compute values of confinement and propulsion
    Confinementx = 2*Nx(s)*(beta*h+mu*(Nx(s)*xdot+ydot*Ny(s)))
    Propulsionx = 8*alpha*Vp**2*Ny(s)**3*(-xdot*Ny(s)+ydot*Nx(s)-Vp)
    Confinementy = 2*Ny(s)*(beta*h+mu*(Nx(s)*xdot+ydot*Ny(s)))
    Propulsiony = 8*alpha*Vp**2*Nx(s)**3*(-xdot*Ny(s)+ydot*Nx(s)-Vp)

    # Compute values of xddot and yddot (Einstein summation by abuse of notation)
    xddot = -C[0,i,j]xdot^i xdot^i - Confinementx - Propulsionx
    yddot = -C[1,i,j]xdot^i xdot^i - Confinementy - Propulsiony

    return [xdot,ydot,xddot,yddot]


# First initial guess of (s,h) with kd-tree
(s0,h0) = phi_inv(xi,yi)
d = dict(s=s0,h=h0) # Store initial guess for first time step

# Define noise matrix
def Noise(x,t):
    return np.diag([0.0, 0.0, sigma, sigma])

# Solve system of SDE's with initial values with SRI2 scheme
solution = sdeint.itoSRI2(model, Noise, initial values, evaluation time)
```

Figure C.1: Pseudo-code for the simulations of the proposed model. The procedure is explained in Chapter 5 and the model is explained in Chapter 4.